PHYSICAL REVIEW A VOLUME 48, NUMBER 1 JULY 1993

Measurement of the positronium $1\,^3S_1-2\,^3S_1$ interval by continuous-wave two-photon excitation

M. S. Fee* and S. Chu
Physics Department, Stanford University, Stanford, California 94305

A. P. Mills, Jr., R. J. Chichester, and D. M. Zuckerman
AT&T Bell Laboratories, Murray Hill, New Jersey 07974

E. D. Shaw
Physics Department, Rutgers University, Newark, New Jersey 07102

K. Danzmann
Max Planck Institute für Quantenoptik, Garching 8046, Germany

(Received 2 October 1992)

Positronium is the quasistable bound system consisting of an electron and its antiparticle, the positron. Its energy levels can be explained to a high degree of accuracy by the electromagnetic interaction, affording an ideal test of the quantum electrodynamic (QED) theory of bound systems. We have measured the $1\,^3S_1-2\,^3S_1$ interval in positronium by Doppler-free two-photon spectroscopy to be $1\,233\,607\,216.4\pm3.2$ MHz. We employ continous-wave (cw) excitation to eliminate the problems inherent with pulsed laser measurements of nonlinear transitions. Positronium (Ps) atoms generated in vacuum are excited to the 2*S* state using cw laser light built up to 2.5 kW circulating power in a resonant Fabry-Pérot cavity. The excited-state atoms are photoionized using a pulsed laser at 532 nm, and the liberated positrons counted as the cw laser is tuned relative to a reference line in tellurium (Te_2) molecular vapor. The fit of a detailed theoretical model to the measured line shape determines the Ps resonance frequency relative to the Te_2 reference line. The Monte Carlo model includes details of the excitation and detection geometry, the Ps velocity distribution, and the dynamic Stark shift, and gives excellent agreement with the measured line shapes. The quoted 2.6 parts per billion (ppb) uncertainty is dominated by the measurement of the Ps line center relative to the Te_2 reference line, with a 1.0-ppb contribution from a recent calibration of our Te_2 cell relative to the hydrogen 1*S*-2*S* transition frequency. The measurement is in excellent agreement with theory and sufficiently accurate to provide a test of the as-yet-uncalculated α^4R_∞ QED correction. Our measurement tests the α^2R_∞ QED contributions to the energy of the $1\,^3S_1$ and $2\,^3S_1$ states to 3.5 parts in 10^5.

PACS number(s): 36.10.Dr, 12.20.Fv, 32.80.Fb

I. INTRODUCTION

Positronium (Ps) is a quasistable atom composed of an electron and its antiparticle, the positron. It is one of a family of leptonic hydrogenlike systems that includes muonium (μ^+e^-), and tauonium (τ^+e^-). Ps is also one of a family of more exotic particle-antiparticle systems such as "muium" ($\mu^+\mu^-$), and "protonium," a proton-antiproton bound state whose Lyman and Balmer series has recently been observed in the x-ray region [1]. Of these, only Ps, muonium, and tauonium have energy levels accessible to laser excitation, and only Ps and muonium have been produced in sufficient quantity to do laser spectroscopy [2,3].

Whereas hydrogen is composed of an electron and three quarks interacting through the strong, weak, and electromagnetic forces, Ps is composed simply of two leptons. A nearly complete description of Ps is possible with the electroweak interaction, and to high accuracy by the electromagnetic interaction alone, affording an ideal test of quantum electrodynamics. The simplicity of the positronium atom itself does not have its equal in the theoretical framework within which it is described. In a nonrelativistic system, the interaction of two equal-mass particles can be reduced to a one-body problem in a center-of-mass frame through a simple Galilean transform. The Hamiltonian is then written using the reduced mass of the particles. The Ps atom, however, is relativistic at the level of $E_I/2m_ec^2\approx10^{-5}$, where $E_I=6.8$ eV is the Ps binding energy, and cannot be reduced in a simple way to a one-body problem.

In contrast, although H also has relativistic corrections, the large proton-to-electron mass ratio allows one to calculate the fine structure to first order with the Dirac equation, by considering the electron in a fixed Coulomb potential. Nonrelativistic reduced-mass corrections are included as a modification of the value of the Rydberg constant, and relativistic reduced mass, or relativistic "nuclear recoil," corrections may subsequently be applied as perturbations to the Dirac energy levels. In Ps, however, the Dirac equation fails completely, and even to first order one must resort to a relativistic two-particle equation to obtain the fine structure. Bethe and Salpeter [4] and Schwinger [5] developed the basic field-theoretic equation describing the relativistic two-body problem; unfortunately the Bethe-Salpeter equation has no exact solutions, even in lowest order.

A two-body formalism applicable to positronium and muonium has more recently been introduced by Lepage and Caswell [6] and Remiddi and Barbieri [7]. They have succeeded in transforming the Bethe-Salpeter equation to an equivalent one-body Dirac equation, resulting in analytical solutions to lowest order. The higher-order solutions to this transformed equation are essentially nonperturbative. Although they involve integrals, called kernels, that can be expressed in terms of Feynman diagrams, the fine-structure constant α does not enter the wave functions and propagators in a perturbative way as it does for other precision calculations such as the magnetic moment of the electron. Despite this difficulty, theorists are still able to use small parameters such as α to develop expressions of decreasing magnitude for succeeding corrections. The nonperturbative character of the expansion is revealed by the appearance of logarithmic factors, resulting in an expansion such as R_∞, $R_\infty\alpha^2$, $R_\infty\alpha^4\ln\alpha$, $R_\infty\alpha^3$, $R_\infty\alpha^4\ln\alpha$, $R_\infty\alpha^4,\ldots$, where the Rydberg constant is $R_\infty=\alpha^2mc/2h$. This approach allows a rough estimate to be made of the magnitude of the neglected terms, and therefore of the accuracy of the calculation. Unfortunately, there is no reliable means of estimating the size of the coefficient associated with an uncalculated term.

The particle-antiparticle nature of positronium has a clear impact on the difficulty of the calculations at each order of the calculation. The $R_\infty\alpha^3$ calculation in H has a contribution from only two Feynman diagrams, as compared to ten for Ps, seven of which are due to virtual annihilations. However, two-photon virtual annihilation terms do not contribute to the energy of the Ps triplet states by C-parity conservation. Multiphoton virtual annihilation first appears in the $R_\infty\alpha^4$ correction for the triplet states. The calculation of $R_\infty\alpha^4$ correction involves hundreds of Feynman graphs and is clearly difficult, but this must be offset by the fact that positronium is the only experimentally accessible system in which self-annihilation terms may be tested by precision measurements. Because the positron and electron have equal masses, Ps is also the most sensitive system in which to test the quantum-electrodynamic (QED) relativistic two-body formalism.

Currently, the coefficients for the terms in the expansion given above have been calculated for the triplet states through $R_\infty\alpha^4\ln\alpha$. The expansion for the $n\,^3S_1$ states has the following form:

$$\frac{E(n\,^3S_1)}{h}=-\frac{1}{2n^2}c(R_\infty)+2\frac{1}{n^3}c(R_\infty\alpha^2)\left[\frac{11}{64}\frac{1}{n}-\frac{1}{2}\right]-\frac{6}{4\pi}\frac{1}{n^3}c(R_\infty\alpha^3\ln\alpha)$$
$$+\frac{1}{4\pi}\frac{1}{n^3}c(R_\infty\alpha^3)\left\{\frac{14}{3}\left[\frac{7}{15}+\ln(2/n)+\frac{n-1}{2n}+\sum_{k=1}^{n}k+\ln 2\right]-\tfrac{16}{3}\ln k_0(n)\right\}-\frac{1}{6}\frac{1}{n^3}c(R_\infty\alpha^4\ln\alpha)\,, \qquad (1)$$

where $\ln k_0(n)$ are the Bethe logarithms [8]. The first term in Eq. (1) is simply the result of the nonrelativistic Schrödinger equation, using the Ps reduced mass as discussed earlier. The $R_\infty\alpha^2$ term was calculated by Ferrell [9]. The $R_\infty\alpha^3\ln\alpha$ and $R_\infty\alpha^3$ terms were calculated together for the $n=2$ levels by Fulton and Martin [10] and later generalized by Fulton to the $n=1$ levels with the erroneous assumption of a $1/n^3$ scaling law for this term [11], as noted and corrected by several authors [12,13]. Finally, identical results have been reported for the $R_\infty\alpha^4\ln\alpha$ correction by Fell [14] and Khriplovich, Milstein, and Yelkhovsky [15]. Table I shows the frequency contribution of each of these terms to the $1\,^3S_1$ and $2\,^3S_1$ levels, and to the $1S$-$2S$ transition. Work is in progress to calculate the $R_\infty\alpha^4$ correction, which will have a contribution of $cR_\infty\alpha^4=9.6$ MHz if the coefficient is unity.

Positronium decay rates have been a subject of much recent theoretical and experimental interest as a test of QED calculations [16]. As a matter-antimatter system, positronium is subject to annihilation into two or more γ photons. Large differences between the lifetimes of the singlet and triplet series result from conservation of charge-conjugation (C) symmetry, which implies that the

TABLE I. QED corrections to $1\,^3S_1$ and $2\,^3S_1$ levels and $1\,^3S_1$–$2\,^3S_1$ transition frequency, in MHz.

Order	$\Delta\nu(1\,^3S_1)$	$\Delta\nu(2\,^3S_1)$	$\Delta\nu(2\,^3S_1-1\,^3S_1)$
R_∞	−1 644 920 980.6	−411 230 245.1	1 233 690 735.41
$R_\infty\alpha^2$	89 419.2	7413.6	−82 005.59
$R_\infty\alpha^3\ln\alpha+R_\infty\alpha^3$	1733.1	231.7	−1501.44
$R_\infty\alpha^4\ln\alpha$	7.6	1.0	−6.69
Total	−1 644 829 820.6	−411 222 598.9	1 233 607 221.7

singlet states decay into an even number of γ rays, while the triplet states decay into an odd number of γ rays. Each additional photon involved in a decay process decreases the likelihood of the decay by a factor of order α. Since conservation of energy and momentum forbids the decay of Ps into one γ, the triplet states decay primarily into three photons and the singlet states decay into two photons. Singlet decay into four photons has recently been observed [17].

The most accurate measurement of the triplet ground-state lifetime, to the level of 230 ppm, has recently been made by Nico *et al.* [18]. QED corrections to the Ps triplet ground-state decay rate, calculated with the Lepage formalism to order $\alpha^2\ln\alpha$ [19,20], are currently in disagreement with experiment by six standard deviations of the experimental result. QED and exotic non-QED explanations have been proposed for the discrepancy. It has been argued [18], however, that the discrepancy will be accounted for by an unusually large coefficient for the next higher-order α^2 QED correction. The measurement of the $1\,^3S_1-2\,^3S_1$ interval we report here will test radiative corrections at the same order as those appearing in the α^2 QED lifetime correction, providing a point of contact between the lifetime and energy-level measurements. For a review of advances in precision experiment and theory see Refs. [16] and [13].

The technique of Doppler-free two-photon spectroscopy was proposed by Vasilenko, Chebotayev, and Shishaev [21], by which an atom may be excited by two photons from an initial state to a final state with the same parity, for example from the 1*S* state to the 2*S* state of a hydrogenlike atom. The use of counter-propagating laser beams, although not necessary for two-photon excitation, affords two distinct advantages. When a moving atom absorbs one photon from each of the two beams, the two photons, as seen in the rest frame of the atom, have Doppler shifts that are the same in magnitude, but of opposite sign. To first order in velocity the sum of the frequencies of the two photons is the same in all moving frames, and there is no Doppler broadening. The absorption of two photons of the same *k* vector may occur with linearly polarized excitation beams and will excite a very small fraction of the atoms with a Doppler-broadened profile. The second advantage of the two-photon transition is that when the laser frequency is near the atomic resonance frequency, *all* atoms within the laser volume will be excited, an essential feature with the low Ps production rates available.

The selection rules for the two-photon transition have been discussed in detail by Cagnac, Grynberg, and Biraben [22]. Applied to the 1*S*-2*S* transition, the transition selection rule is that $\Delta J=0$ and $\Delta M_J=0$. Basically, because the intermediate P states are far from resonance, the spin structure (fine and hyperfine) is only relevant to the transition probability at the $\sim 10^{-6}$ level and the important paths for 1*S*-2*S* excitation are indistinguishable from those of an atom made of spinless particles. The consequence is that only transitions between identical M_J levels are allowed, and all have equal oscillator strengths. A second consequence is that 1*S*-2*S* excitation by $\sigma^+\sigma^+$ circularly polarized beams of the same angular momentum, such as one finds in an ordinary build-up cavity driven by circularly polarized light, violates conservation of angular momentum and is highly suppressed. The excitation beams must be either linear polarized, or circularly polarized in such a way that photons in the counter-propagating beams have opposite angular-momentum vectors ($\sigma^+\sigma^-$). The $\sigma^+\sigma^-$ configuration requires that a quarter-wave plate be used in conjunction with each retroreflection, and is presently incompatible with cw excitation in a low-loss build-up cavity.

The 142-ns lifetime of the $1\,^3S_1$ state and the 1.1-μs lifetime of the $2\,^3S_1$ state combine to yield a 1.26-MHz natural linewidth for the $1\,^3S_1-2\,^3S_1$ transition, or one part in 10^9, making this transition ideal for precision spectroscopy. It is unfortunately difficult to achieve this resolution in the measured line shape. The small mass of the Ps atom results in mean thermal velocities of 10^7 cm/s at 600 K, the second-order Doppler shifts due to relativistic time dilation, given by

$$\nu_d=(v^2/2c^2)\Delta\nu(1\,^3S_1-2\,^3S_1)\ ,$$

corresponding to tens of MHz.

Chu and Mills used the two-photon Doppler-free transition to observe the $1\,^3S_1-2\,^3S_1$ transition in Ps [23] with a resolution of 1 ppm. Chu, Mills, and Hall [2] then measured this transition to be 1 233 607 185±15 MHz. Roughly half of the 12 ppb error estimate was due to the determination of the positronium line center relative to their secondary frequency standard, a line in tellurium vapor. The remainder of the error estimate was attributed to the calibration of the tellurium standard to the deuterium $2S_{1/2}$-$4P_{3/2}$ Balmer line. The 1*S*-2*S* measurement in Ref. [2] was found to be in good agreement with the $R_\infty\alpha^3$ QED corrections [11], the two differing by 13±15 MHz.

However, a subsequent recalibration of the Ps reference line in Te_2 by McIntyre and Hänsch [24] corrected the Ps transition frequency to the red by 42 MHz to 1 233 607 142.9±10.7 MHz, a value 56.4±10.7 MHz smaller than Fulton's theoretical value [11]. Then an error was discovered in the sign of the pulsed laser frequency offset in the measurement of Chu, Mills, and Hall [2] and published later by Danzmann, Fee, and Chu [31], with the latest (prior to the present measurement) value of the transition frequency of 1 233 607 218.9±10.7 MHz, 16.6±10.7 MHz above the corrected theoretical value. Finally, Fell's $R_\infty\alpha^4\ln\alpha$ QED corrections once again eliminated discrepancy between theory and experiment. There remained, however, the clear need for further advances in the measurement and theory of the 1*S*-2*S* interval in positronium.

Because of the large intermediate state detuning of the 1*S*-2*S* two-photon transition, high intensities are required to drive the transition, so precision measurements in hydrogen [25] and positronium [2] have been made using narrow-band pulsed lasers produced by amplifying a cw "seed" laser with a series of traveling-wave amplifiers. Pulsed lasers are usually characterized in terms of their temporal and spectral intensity profiles. Any frequency fluctuations appear as a spectral broadening of the laser output, which may be expressed by the degree to which the linewidth of the laser exceeds the lower limit dictated by the Fourier transform of its pulse envelope. Apart from picosecond and femtosecond lasers, where the pulses can actually be very close to the Fourier-transform limit, most pulsed lasers fall short of achieving the minimum uncertainty in $\Delta\nu\,\Delta t$. The process of amplifying a pulsed laser inherently involves rapid changes in the gain. By the Kramers-Kronig relations, the index of refraction of the amplifying medium is rapidly modulated, resulting in fluctuations of the laser frequency within a single pulse. Measurements of the spectral broadening from the induced frequency modulation do not tell us the instantaneous frequency (the time derivative of the instantaneous phase of the complex amplitude) of the pulse. Knowledge of the time evolution of the phase is essential to thoroughly predict or interpret the results of several types of experiments, particularly the spectroscopy of nonlinear transitions. This limitation was recognized and discussed by Wieman and Hänsch [26], and was the principal uncertainty in their measurement of the hydrogen $1S$ Lamb shift.

In general, one would not attempt to make a precision measurement with a pulsed laser as it appears at the output of the amplifier, for exactly the reasons outlined above. In the pulsed measurements of H and Ps, the laser light was filtered in a Fabry-Pérot interferometer before being used to excite the atoms, the assumption being that the filtered light had sufficiently small frequency chirps as to be neglected. In general, this assumption is incorrect as has been shown by an experimental measurement of the instantaneous frequency behavior of an excimer-pumped dye-laser system [27] (the same one used in the muonium measurement [3]). The output of the laser amplifier was filtered in a Fabry-Pérot interferometer and mixed at a detector with a frequency-shifted sample of the cw seed light, and the resulting beat note measured. The instantaneous frequency behavior was then extracted from the beat signal using Fourier-transform techniques. We find that pronounced frequency chirps are possible even after the filtering process. The effect of such frequency chirps on the resulting two-photon line shape was modeled, indicating that laser frequency chirps contributed roughly ±2 MHz uncertainty to the measurement of Ref. [2] of the $1S$-$2S$ interval in positronium.

By directly measuring the phase behavior of traveling-wave pulsed amplifiers, precision pulsed measurements of nonlinear transitions to the level of 1 MHz may be possible. However, several factors led us to abandon this approach in favor of a continuous-wave measurement. The possibility of an intense, cryogenic (50 K) positronium source [28] raised the cw excitation rate (proportional to $1/T$) to an acceptable level. Additionally, the availability of ultralow-loss laser mirrors at 486 nm [29] prompted us to construct the required apparatus to frequency stabilize our Coherent 699 dye laser to the kilohertz wide resonance of an ultrahigh-finesse cavity [30], eventually allowing us the generate more than 2.5 kW cw circulating laser power.

Using the result our recent calibration of the frequency of the tellurium reference line of 616 803 544.4(6) MHz, we obtain a result for the $1\,^3S_1-2\,^3S_1$ interval in positronium of $1\,233\,607\,216.4\pm3.2$ MHz. We are in agreement with the most recent $R_\infty\alpha^4\ln\alpha$ QED corrections [14,15] yielding a theoretical value for the $1S$-$2S$ interval of $1\,233\,607\,221.7\pm O(10)$ MHz. Our measured value is 2.5 MHz lower than the corrected value of the Chu-Mills-Hall [2] measurement [31], and represents a factor of 3.3 improvement in the accuracy.

The precision of the measurement reported in this paper is sufficient to test the as-yet-uncalculated $R_\infty\alpha^4$ QED corrections to both the excited and ground states, which is on the order of 10 MHz. The uncertainty of our measurement corresponds to 3.5×10^{-5} of the α^2R_∞ QED contribution to the $1\,^3S_1-2\,^3S_1$ interval. Our experimental result also represents a factor-of-3 improvement in the constraint on the positron-electron mass ratio [32], and is a factor of 50 more stringent than a recent constraint based on the electron-positron cyclotron frequency ratio [33], assuming equal charges.

II. EXPERIMENT

A schematic overview of the experimental apparatus is shown in Fig. 1. Positrons generated at the beam dump of a free-electron laser are collected in an electromagnetic bottle and bunched into a 25-ns pulse at the positronium source [34]. Ps atoms are then generated in vacuum at the atomically clean surface of a pure aluminum crystal [(111) plane]. Approximately 30% [35] of the incident positrons are thermally desorbed from the 576-K surface as positronium atoms with a beam-Maxwellian velocity distribution (Sec. II A). A cw laser beam built up to a circulating power of 2.5 kW by a resonant Fabry-Pérot cavity is placed 1.5 mm in front of the Al target to excite the $1S$-$2S$ transition. After a variable time delay between 50 and 200 ns during which the Ps atoms drift ballistically through the cw excitation beam, excited-state atoms are photoionized a few millimeters from the target using a neodymium-doped yttrium-aluminum-garnet (YAG) pulsed laser. The e^+ photoionization fragments are accelerated out of the laser interaction region with an ~2 V/cm electric field, through a constant potential drift tube, to a channel electron multiplier array (CEMA). Detected positrons are counted as the laser is tuned relative to the Ps line center. We discuss details of the laser excitation and detection geometry in Sec. II B.

The majority of the cw laser power is delivered to the build-up cavity in a small bandwidth using a frequency-modulation locking scheme [36]. The laser is locked to the cavity resonance by rapidly correcting the laser frequency with an intracavity phase modulator inside the ring dye laser. Details of the build-up cavity and locking scheme are discussed in Secs. II C and II D, respectively. As discussed in Sec. II E, the tuning of the cw dye laser and build-up cavity is generated as a radiofrequency offset to ensure the accuracy and linearity of the frequency scan. A small fraction (25 mW) of the cw laser power is frequency offset using rf-driven acousto-optic modulators. The frequency-shifted light is sent to a frequency-modulated saturated absorption spectrometer [37,38] which yields a dispersive-shaped line suitable as an error signal for a frequency lock. The servo loop is closed by connecting the frequency-modulation (FM) spectrometer output to the input of the voltage-controlled rf oscillator (VCO). The acousto-optic modulators (AOM's) are thus tuned so that the frequency-shifted light is locked to the center of the Te_2 resonance. Simply by counting the rf frequency of the VCO, we know the cw dye-laser frequency accurately relative to the Te_2 reference line. The piezoelectric elements of the build-up cavity are tuned to achieve the desired laser frequency.

A small fraction of the laser power (10 mW) is used for simultaneous saturation spectroscopy [39,40] of a recently calibrated reference line in tellurium molecular vapor (Te_2). We use the e_3 component of Ref. [24], which has a frequency approximately 65 MHz below the Ps $1S$-$2S$ transition frequency. Details of the tellurium reference and our calibration of the e_3 line relative to the hydrogen $1S$-$2S$ transition are contained in Sec. II F.

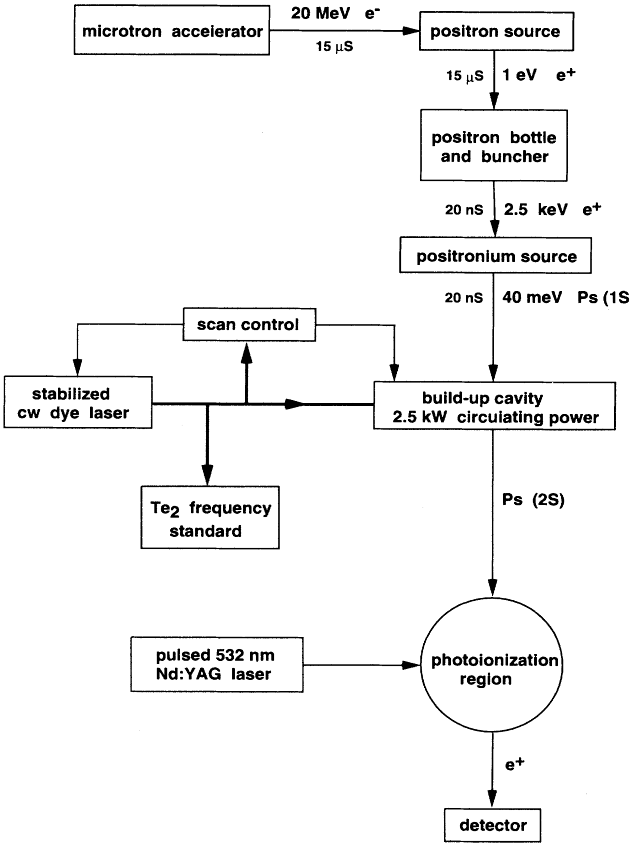

FIG. 1. Schematic overview of the complete experiment. The positron source is located at the beam dump of a microtron accelerator. The positrons are moderated to 1 eV energies and trapped in a magnetic bottle. A parabolic accelerator bunches the trapped positrons to a 25-ns pulse onto an Al single crystal, where thermal Ps atoms are generated in vacuum. The Ps source is located inside a cw laser build-up cavity with a finesse of 10^5 and circulating power of 2.5 kW. The Ps atoms that pass through the cw 486-nm laser beam are excited to the $2S$ state and subsequently photoionized by a 532-nm pulsed Nd:YAG laser. The e^+ photoionization fragments are collected at a single-particle detector and counted as a function of cw laser frequency.

A. Positronium source

A vacuum source of Ps begins with energetic positrons, which in the previous experiment were provided by β^+ emitting ^{58}Co. The disadvantage of such a source is that it is inherently continuous, and therefore requires long storage times to produce a pulsed e^+ beam. Recent advances in high intensity, accelerator based, pulsed positron sources has provided up to 10^9 positrons per second [41]. In our measurement, we used the beam dump of the AT&T Bell Laboratories free-electron-laser facility as a source of energetic positrons. The apparatus is discussed in detail by Mills *et al.* in Ref. [34]. Electrons are accelerated in a microtron accelerator to 20 MeV in 16-μs pulses at a 30-Hz repetition rate, greatly reducing the required storage time. The peak and average electron currents were 40 mA and 20 μA, respectively. The relativistic electrons impinge on a 3.8-mm-thick sintered tungsten target to produce energetic positrons in a shower of bremsstrahlung and pair-production processes.

The relativistic positrons so produced are not directly useful for positronium production. They must first be slowed and then transported to a region away from the intense radiation at the beam dump. The relativistic positrons impinge on a moderator, typically a metal crystal of tungsten [42–44]. Upon implantation into the metal, the positrons quickly thermalize with the electrons and can diffuse over a distance of about 1000 Å back to the surface. The positrons see a dipole potential at the surface of the metal, due to the electron wave functions extending past the lattice of metal ions, that tends to expel them from the surface. As the positrons leave the metal, they are accelerated normal to the surface to a few eV kinetic energy. Yields of up to 0.2% have been measured with a radioactive source and a well-annealed tungsten moderator [44].

In our measurement, the positrons are moderated by a 9-mm-diam, 6-mm-thick W(110) single crystal placed 1 mm from the tungsten target. The crystal was prepared by heating to 2000 K *in situ* to anneal out defects which trap diffusing slow positrons, and must be reannealed every few hours of operation due to radiation damage. The slow positron efficiency is 4×10^{-8} positrons per 20 MeV electron. A 150-G magnetic field guides the positrons through tungsten shielding blocks and a brick and lead wall required to protect the experimental area from the intense radiation at the target.

The relatively long pulse of slow positrons is trapped in a magnetic bottle and bunched into a short pulse using a parabolic potential accelerator [23,45]. The positrons are trapped after passing through the pinched magnetic field at the entrance to the magnetic bottle by a transverse rf electric field tuned to the positron cyclotron-resonance frequency of 430 MHz. The slow positrons then pass into a 2-m-long accelerator tube consisting of a series of 100 stainless-steel rings connected to a resistor network.

During the bottle phase of the cycle, the rings are held at ground potential, and one of the rings near the far end of the accelerator tube is held at $+15$ V to electrostatically reflect the incident positrons. The reflected positrons pass again through the 430-MHz transverse electric field, and are reflected by the pinched magnetic field due to their large transverse energy. After the 16-μs slow positron pulse, the bottle has been loaded, and the end of the accelerator tube nearest the rf plates is pulsed to a potential of 2500 V in 10 ns. The resistor network is designed such that the accelerator tube then acquires a parabolic potential, and all of the bottled positrons reach the bottom of the potential in one-quarter of a harmonic period. The positrons are thus bunched into 25-ns pulses at 30 Hz, each containing $\sim 5\times10^4$ slow positrons. The efficiency of the bottle and buncher is 63%.

The production of thermal positronium atoms from a slow e^+ beam is an essential aspect of many precision measurements in Ps, and the process has been considered in detail both theoretically and experimentally [44]. As for positron moderation, positrons implanted in a metal with several keV of energy will thermalize with the electrons and begin to diffuse in the metal. If the metal is a single crystal with few defects, the positrons have a large diffusion length before they annihilate, and most of the positrons diffuse to the surface where they experience the surface dipole layer. Once the positron leaves the surface, its image creates a potential attracting it back to the surface of the metal. The positron may either fall into the potential well by the creation of a phonon or electron-hole pair, or it may simply leave the surface as a remoderated, or "reemitted" positron. The e^+ that falls into the potential may either annihilate or be ejected from its surface state by thermal fluctuations, with a high probability of carrying off an electron as a ground-state Ps atom [46].

Mills and Pfeiffer have made measurements of the velocity distribution normal to the surface [35], and found good agreement with a beam-Maxwellian distribution. Using detailed balance, an interesting conclusion can be drawn from this distribution: the reflection coefficient for thermal Ps impinging on the metal surface from outside is independent of velocity [35,47–49].

In our experiment, the bunched positrons are guided by the axial magnetic field to a clean, 99.999% pure Al(111) sample where they are implanted with 1–2-keV kinetic energy to an average depth of $\sim 10^3$ Å. On a time scale less than the $\sim$160-ps lifetime of positrons in the metal, and much less than the bunched e^+ pulse width, an implanted positron diffuses back to the surface of the crystal. We use a single-crystal Al target since the diffusion length is $\sim$1000 Å, orders of magnitude larger than in polycrystalline Al. The (111) face of Al was chosen because of its positive positron affinity, reducing the number of reemitted positrons. Even so, about 10% of incident positrons are ejected from the surface with 0.1 eV energies prior to thermalizing in the metal. About 30% leave the surface as thermal positronium with a beam Maxwellian velocity distribution. Prior to taking data, we ion bombarded the Al target for 1 h, then annealed at 615 °C for 10 min to eliminate dislocations that trap the thermalized positrons in the metal. The target was then raised into the focus of an Auger spectrometer for diagnosis of surface contamination. The Al crystal was found to have typically less than 0.1% of a monolayer of sulfur, 1.5% of a monolayer of carbon, and 1% of a monolayer of oxygen. For 15 experimental runs, we kept the sample at 303±5 °C to thermally desorb the surface-state positrons as free thermal Ps in vacuum [2,48].

For seven experimental runs, we cooled the sample to 235±5 °C following ion bombardment and annealing. At the lower temperature, thermal adsorption is greatly enhanced over that from the clean crystal by the addition of roughly 0.25 monolayers of O to the surface. Therefore, we leaked oxygen gas into the vacuum can at 5×10^{-8} Torr for 5 min. In this case, about 10% of the incident positrons have been reported to leave the surface as thermal positronium with a beam Maxwellian velocity distribution [28]. However, during the seven experimental runs done at 235 °C, we saw no evidence of thermal positronium by 1*S*-2*S* two-photon excitation, despite an initially clean surface according to the Auger spectrum. The oxygenation procedure was similar to that of Ref. [28] with the exception that we monitored the Ps three-photon ionization signal using a 30-mJ, pulsed 486-nm laser beam during the process. Scattered light from the pulsed beams could easily have resulted in 1–100 photons/Å^2 on the Al surface. One explanation for the lack of thermal Ps is that photolysis of chemical bonds between physisorbed oxygen and the Al surface destroys the desired surface state in much the same way that heating the target after the oxygenation procedure does.

B. Excitation and detection geometry

Some fraction of positronium atoms desorbed from the Al sample pass through the cw excitation beam placed in front of the target and are excited to the 2*S* state. The technique of detecting these few excited-state atoms per second has undergone several refinements since the original measurement of the 1*S*-2*S* interval in Ps [2]. The result is a reduction in noise by a factor of roughly 10^5 per incident e^+ over the previous measurement, with a comparable signal positron collection efficiency. We observed a background count rate as low as one count per minute (10^8 incident positrons), yielding a maximum signal-to-noise ratio of 60 to 1.

In the previous measurement, the 2*S* positronium atoms excited by the counter-propagating 486-nm pulsed light were detected by subsequent photoionization in the same 486-nm beams. However, at the low intensities available for cw excitation, the photoionization of the 2*S* state is no longer saturated, making resonant three-photon ionization an inefficient method to detect the excited-state atoms. In addition, because of the velocity spread of the Ps atoms, with cw three-photon ionization there would be no clear time window which the signal could be detected. For these reasons, we have decided to use a separate high-intensity laser pulse at 532 nm, the second harmonic of a Nd:YAG (yttrium aluminum garnet) laser to photoionize the excite-state atoms. The laser pulse is passed several times through the volume containing the excited-state atoms. As shown in Fig. 2, the photoionization region is to the left of the cw beam, approximately 6 mm wide and 10 mm deep (into the figure). The geometry of the photoionization region will be discussed in more detail in Sec. III A. We calculate that the 30-mJ, 7-ns pulses result in $\sim 50\%$ ionization probability for excited-state Ps.

The excitation and collection geometry has also been modified from the previous 1*S*-2*S* measurement. In that experiment, as in the one we report here, an axial magnetic field was used to simplify the positron optics. In the previous experiment, the laser excitation region was placed directly in front of the positronium source. Collection of the photoionized signal positrons from the excitation region was accomplished by $\mathbf{E}\times\mathbf{B}$ deflection of the signal positrons to the side of the target, where they were accelerated axially to a time-resolved channel-electron-multiplier-array (CEMA) detector. Subsequent $\mathbf{E}\times\mathbf{B}$ plates were required to energy resolve the reemitted positrons to prevent them from both contaminating the signal and saturating the CEMA.

However, with the small number of excited-state Ps produced with cw excitation, the reemitted positrons represent an overwhelming background; there are roughly 10^4 reemitted positrons for each photoionized signal positron. Despite exhaustive efforts to isolate signal positrons from reemitted positrons using pulsed grids, energy resolution, and CEMA time resolution, the cw excitation signal was several orders of magnitude below the noise.

The new excitation and collection geometry we finally adopted, shown in Fig. 2, includes several features. First, to eliminate the problem with the reemitted positrons, the Ps-laser interaction volume is now split into two separate regions. The upper region contains the incoming positron beam and the Al(111) crystal. Electrically neutral Ps atoms cross magnetic-field lines, through the cw excitation beam, and into the lower region where photoionization of the excited-state Ps and collection of the liberated positrons occurs. The advantage of this arrangement is that signal positrons are collected only from the region below the target, while the reemitted positrons are trapped along magnetic-field lines and are blocked from reaching the detector by the target.

The initially circular, 10-mm-diam incident positron beam is skimmed to produce a flat bottom edge with a 10–90 % width of 1.5 mm. This edge is lined up with the flat bottom of the 1-cm^2 Al(111) target, maximizing the flux of incident positrons at the bottom of the target, while allowing less than 10^{-3} of the incident positrons to hit the CEMA. As shown in Fig. 2, the TEM$_{00}$ mode of the 486-nn build-up cavity is directed along the bottom edge of the target, 1.5 mm from the target surface. Any atom passing through the center of the 486-nm beam will subsequently pass through the photoionization region below and to the left (in the figure) of the target. After the excited-state atom has been photoionized, the liberated positrons are accelerated to the CEMA by an $\sim$2-V/cm axial electric field into a 1-m-long equipotential drift tube to the CEMA, where they are counted. The

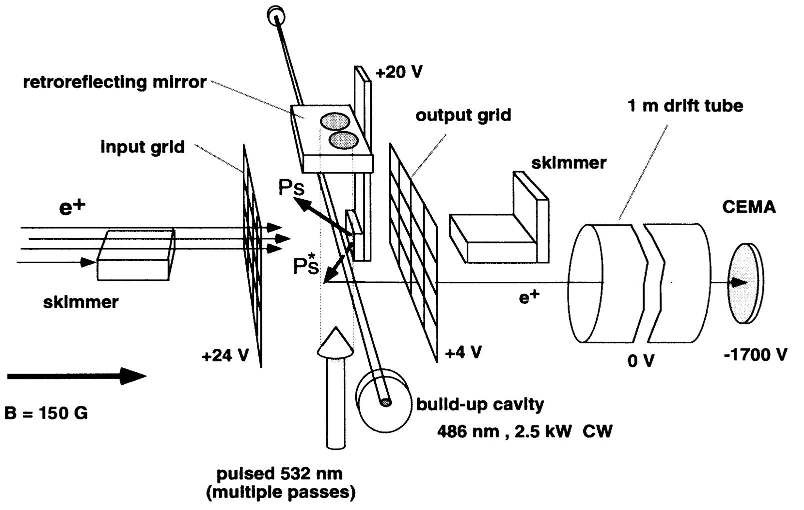

FIG. 2. Positronium source and laser interaction region. The circular, pulsed positron beam enters from the left, guided by a 150-G axial magnetic field. The bottom $\frac{1}{4}$ of the positron beam is blocked by the input skimmer and the flat edge of the beam is aligned with the lower edge of the Al(111) target. Over 10% of the 2×10^4 incident positrons are thermally ejected from the Al target as ground-state (1^3S_1) positronium atoms. Some of these atoms pass through a 2.5-kW cw laser beam formed inside a Fabry-Pérot resonator with a finesse of 10^5, and are excited via Doppler-free two-photon absorption to the $2\,^3S_1$ state. Excited-state atoms cross magnetic-field lines to a region below and to the left of the positronium source, where they are photoionized by a pulsed laser at 532 nm. The two spots on the retroreflecting mirror are due to multiple passes of the 532-nm beam. Approximately one e^+ photoionization fragment per laser pulse is accelerated by an $\sim$2-V/cm electric field along the magnetic-field lines, below the Al target, below a second skimmer, and through a drift tube to a channel electron multiplier array (CEMA) detector. Roughly 400 ns after the photoionization laser fires, the signal positron reaches the detector in a 50-ns time window. The two skimmers work in combination to reduce the number of background positrons reaching the CEMA.

drift tube delays the arrival of the signal positrons relative to the higher-energy background positrons. The dc electric field is generated by highly transparent grids (95% transmission) attached to the quartz support rods of the Fabry-Pérot build-up cavity. The input and output grids are positioned 1.5 cm in front, and 1 cm behind the Al target, respectively. The potential of the input grid, Al target, and output grid were adjusted to maximize the size of the collected photoionized signal, and minimize the background positrons arriving coincidentally with the signal positrons at the CEMA, and typically had potentials of 24.5, 20, and 4 V, respectively, with respect to the drift tube.

We discovered at this point that much of the remaining background was due to positrons, possibly scattered from the input grid into high-transverse-energy orbits, appearing directly behind and to the sides of the target. The addition of a second skimmer behind the target effectively blocks these stray positrons. We also placed adjustable vertical and horizontal apertures (not shown in Fig. 2) immediately before the CEMA. However, the effectiveness of the apertures at further reducing the background count rate was not entirely clear. Figure 3(b) shows a top view of the positronium spectrometer indicating the placement of the drift tube, the CEMA, and its apertures.

The alignment of the skimmers and apertures required that we obtain a two-photon excitation signal using a pulsed 486-nm laser source. We used an excimer pumped, traveling-wave pulsed-dye amplifier as described in Refs. [3,50]. The injection seed beam is provided by a coherent 699-21 actively stabilized cw ring dye laser. The 40-mJ pulses were directed between the YAG photoionized beams and retroreflected from the YAG mirror in the vacuum chamber. By positioning the 486-nm pulsed beams directly in front of the target, resonant three-photon ionization provided hundreds of counts per second, a sufficient signal with which to quickly align the apparatus.

The alignment procedure was as follows, with all skimmers and apertures initially in the fully open position: First, we positioned the target with respect to the fixed cw laser beam. Second magnetic trim coils allowed us to steer the incident e^+ beam so that the brightest (central) part of the beam was centered horizontally, and positioned on the lower part of the Al target, passing roughly one-third of the incident e^+ below the target to the CEMA. Third, the front skimmer (to the left in Fig. 2)

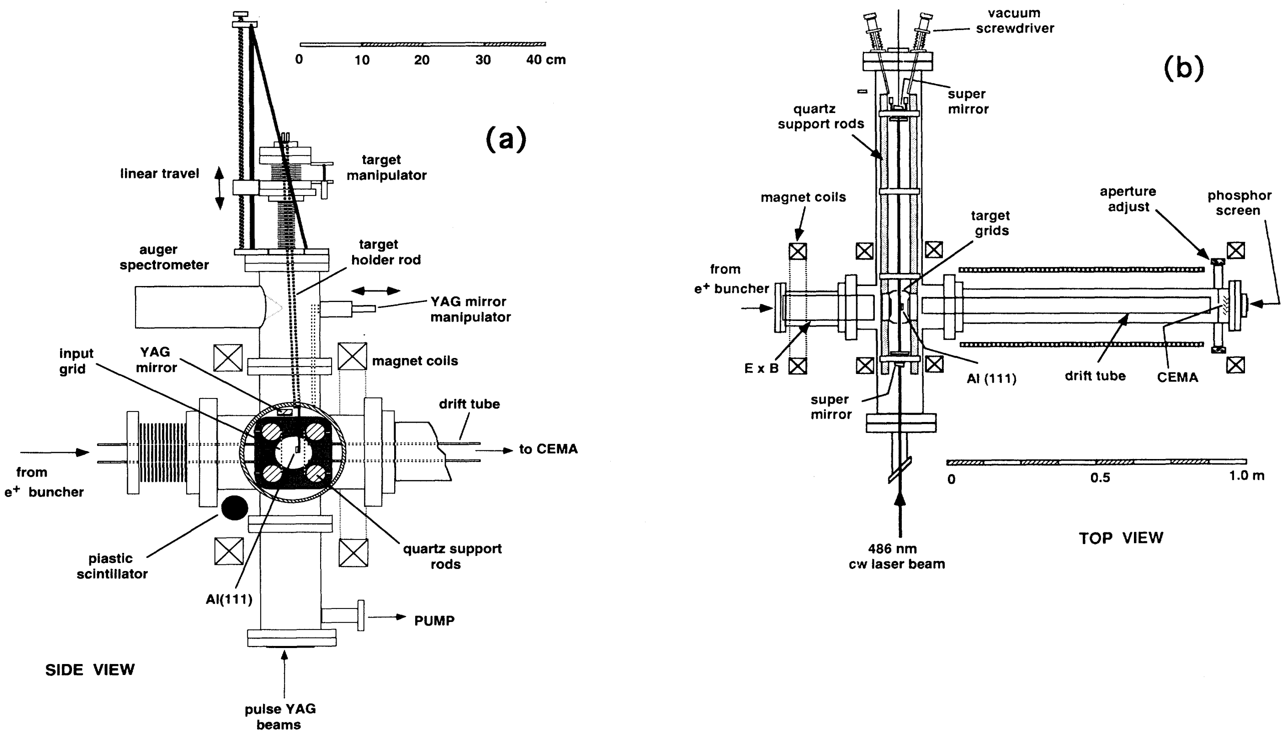

FIG. 3. (a) Side view of the experimental vacuum chamber. At the center is the Al target shown in the beam line and between the quartz support rods of the build-up cavity. The axis of the cw laser beam is into the page. The target may be raised using the linear travel to an Auger spectrometer for surface diagnostics. The multiple passes of the YAG beam enter through an AR coated window at the bottom and are reflected by the dielectric mirror just above the build-up cavity. The mirror can be moved to the left and right by a linear feedthrough. (b) Top view of the experimental chamber showing the 1-m build-up cavity. The cw laser beam enters from the bottom (in the figure) through a Brewster's angle vacuum window. The angle of the output ultralow-loss mirror (super mirror) is adjustable using the vacuum feedthrough screwdrivers. The positrons enter from the left (in the figure) to impinge on the Al target. The photoionized positrons are accelerated to the CEMA through a drift tube to increase the time delay between the prompt higher-energy positrons and the low-energy signal positrons.

was raised to block the transmitted incident positrons until the observed three-photon ionization signal began to fall. It was then lowered so that the ionization signal was suppressed by less than 5%. Fourth, the rear skimmer was lowered until the photoionization signal began to fall, then raised so the photoionization signal was suppressed by less than 5%. The CEMA apertures were opened with calibrated linear vacuum feedthroughs to roughly 1 cm^2 area. With the cw beam in the cavity (no pulsed 486-nm beam), and using the YAG photoionization beam, the target and grid voltages were fine-tuned to maximize the signal to noise.

A plastic scintillator, shown in Fig. 3(a), registered the 25-ns burst of annihilation γ rays from the target area. In addition, we directed a portion of the YAG photoionization laser beam at a small pinhole in the light-tight scintillator housing. The output of the attached photomultiplier tube had two short pulses, a 25-ns pulse due to the γ rays followed by a 15-ns pulse from the 532-nm laser pulse, allowing us to set the relative timing of Ps production and excited-state photoionization with ± 5-ns accuracy. The time spectrum of positrons arriving at the CEMA was recorded for each positron pulse using a LeCroy 9450 digital oscilloscope. The oscilloscope was set in "sequence" acquisition mode, allowing the computer to transfer the time spectra for 100 positron pulses at the end of each 3.3-s interval.

C. Ultrahigh-finesse build-up cavity

The frequency stable source of 486-nm radiation for driving the high-finesse build-up cavity is a Coherent 699-21 actively stabilized cw ring dye laser, shown in Fig. 4. Locking a dye laser to the 1.6-kHz linewidth of our build-up cavity requires a high-bandwidth servo loop. Following the approach in Ref. [30], we have modified our laser by inserting an intracavity phase modulator (Gsanger PM-25) in the dye-laser cavity. By modulating the effective laser cavity length over a 300-Hz to 1-MHz band, we can counteract rapid phase fluctuations caused by the dye jet. The error signal is also summed into the internal locking electronics of the 699-21 control box, providing additional gain from dc to 1 kHz. The frequency stability of the locked cw laser is approximately 100 Hz relative to the build-up cavity resonance.

The major fraction of the cw laser power is reserved for driving the build-up cavity. The piezoelectrically tunable cavity is inside the experimental vacuum chamber,

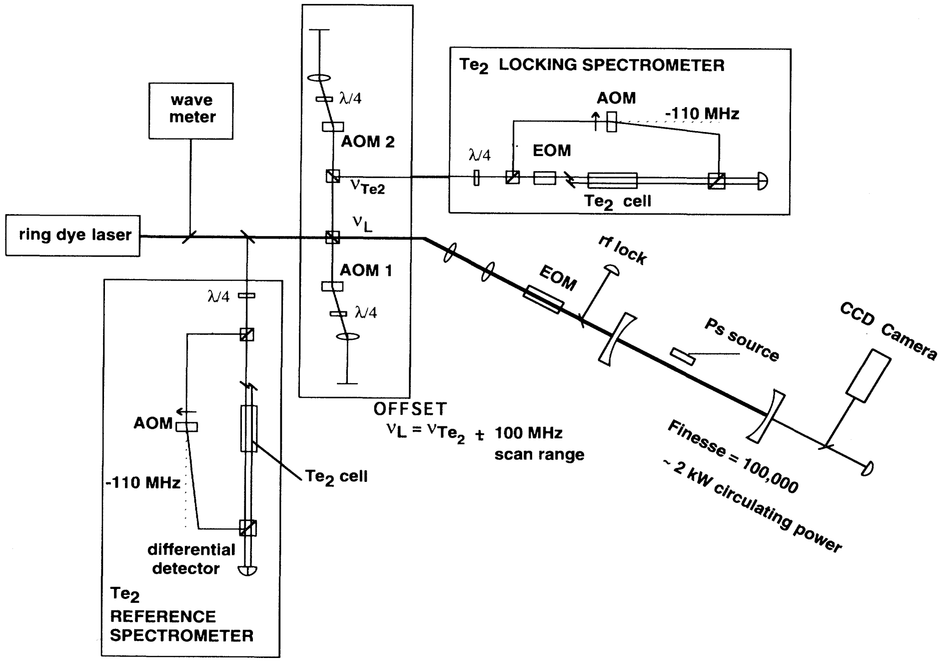

FIG. 4. A ring-dye laser provides up to 400 mW single-frequency radiation at 486 nm. The major fraction of the laser power is used to drive an ultrahigh-finesse build-up cavity to circulating powers of up to 2.5 kW. The laser is mode matched to the TEM_{00} mode of the cavity and is locked to the 2-kHz linewidth of the cavity using the rf sideband locking technique. A temperature-stabilized tellurium saturated absorption spectrometer (labeled Te_2 REFERENCE SPECTROMETER) serves as a frequency reference for the positronium spectroscopy. The 110-MHz acousto-optic modulator (AOM) modulates the pump beam for lock-in detection and also shifts the center of the Te_2 line +55 MHz so that the Te_2 line and the positronium line appear simultaneously during a scan. We direct 20 mW of the laser output through a pair of double-passed AOM's (labeled RF OFFSET). The frequency-shifted beam, tunable from +100 to −100 MHz of the dye-laser output, is used in a frequency-modulated, saturated absorption spectrometer (labeled Te_2 LOCKING SPECTROMETER). The modulation frequency of the AOM's is continuously adjusted to keep the frequency-shifted beam locked on the Te_2 resonance line. Measuring the modulation frequency of the two AOM's gives a direct measure of the rf frequency offset between the tellurium resonance and the dye-laser frequency.

as shown in Fig. 3(b), and has a near-confocal geometry, with 1-m radius of curvature mirrors and a length of 90 cm. The free spectral range is 160 MHz and the transverse mode separation is 8 MHz. The relation between the cavity parameters and the cavity finesse F is

$$F=\frac{2\pi}{A+A'+T+T'}\ , \qquad (2)$$

where A and A' are the absorption and scattering loss of the input and output mirrors, respectively. T and T' are the power transmission of the input and output mirrors, respectively. Using the finesse, we define the cavity reflection as the ratio of power reflected from the cavity on-resonance to the incident power, in the TEM_{00} mode:

$$\frac{P_R}{P_0}=\tfrac{1}{4}(A+A'+T'-T)^2\left[\frac{F}{2\pi}\right]^2 . \qquad (3)$$

It is clear from Eq. (3) that there is an impedance matching condition on the transmission T of the input mirror given by $T=A+A'+T'$, for which the cavity reflection is zero. Similarly, we define the cavity transmission as the ratio of transmitted power on resonance to the incident power:

$$\frac{P_T}{P_0}=TT'\left[\frac{F}{2\pi}\right]^2 . \qquad (4)$$

Finally, we similarly define the build-up of the cavity as the ratio of the circulating power to the incident power:

$$\frac{P_C}{P_0}=T\left[\frac{F}{2\pi}\right]^2 . \qquad (5)$$

One can see that the circulating power in the cavity can be determined directly by measuring the transmitted laser power and dividing by the transmission coefficient of the output mirror T', independent of any other cavity parameters.

We obtained two sets of laser gyroscope quality mirrors. The first set have quartz substrates manufactured by General Optics, Inc., and $\mathrm{TiO_2}$ coatings produced by Ojai Optics, Inc. of Ojai, CA. The Ojai mirrors have a scattering and absorption loss of 20(5) ppm and a transmission of 30(2) ppm. The second set of mirrors we obtained have quartz substrates and $\mathrm{Ta_2O_5}$ coatings, and were manufactured entirely by Particle Measurement Systems (PMS), Inc. of Boulder, CO. The PMS mirrors have a scattering and absorption loss of roughly 15(5) ppm at low laser power. One coating run yielded mirrors with a transmission of 1.86(2) ppm and another yielded mirrors with a transmission of 24(2) ppm. Because of their superior scattering and absorption loss, we attempted to make our measurement with the PMS mirrors, using the 24-ppm mirror at the input and the 1.8-ppm transmission mirror at the output of the cavity. The optic axis of the cavity can be easily aligned by looking through the cavity and adjusting the near mirror so that in it the reflection of one's eye overlaps with the center of the far mirror. The process is repeated for each mirror.

We measure the finesse of our build-up cavity by locking the laser to the TEM_{00} mode of the cavity and acousto-optically gating the dye-laser off for several hundred microseconds. We monitor the transmitted laser intensity with a photodiode to record the exponential decay of the transmitted light on a LeCroy 9450 digitizing oscilloscope. The photodiode is terminated into a 1-kΩ resistor, resulting in a time resolution of a few microseconds. We determined that several successive $1/e$ times of the decay were usually shorter at the higher intensity, but were consistent within 10%. With the PMS mirrors, we measured a cavity ring-down time of $\tau=105$ μs indicating total scattering and absorption losses of 34 ppm. Fluorescence was observed from both mirror coatings at the position of the laser beam, and over the course of the 10 min that the laser was locked to the cavity, the finesse dropped by a factor of 2 to a ring-down time of $\tau=50$ μs (70-ppm losses) and continued to decrease upon further exposure to the high-intensity light. By moving the cavity axis to a new spot on the mirror and using a lower intensity, we determined that the rate of increase in cavity loss was nonlinear in intensity and not simply dose dependent. Since the vacuum was typically better than 10^{-10} torr, it is unlikely that the absorption was caused by contamination from the vacuum. We suspected the input (24-ppm transmission) mirror as the source of trouble, since it had been coated with only a very thin (50 nm) $\mathrm{SiO_2}$ cap layer to reduce scattering losses. Attempts to anneal the damaged mirror at 150 °C failed, as did an effort by PMS, Inc. to repair the unused mirrors with an additional coating of $\mathrm{SiO_2}$.

We replaced the PMS input mirror with an Ojai mirror that had been previously tested with circulating powers of up to 1 kW. With this combination of mirrors, we measured exponential $1/e$ decay times of longer than 100 μs, yielding a cavity resonance width of 1.6 kHz; the ratio of the cavity free-spectral-range (FSR) of 160 MHz to the measured resonance width gives a finesse of 10^5. With the corresponding build-up factor of 7.6×10^3, we obtained circulating powers of up to 2.5 kW before thermal effects distorted the TEM_{00} mode.

The mode size at the position of the target is $w_0=0.31$ mm, giving a peak intensity of $I=1.7$ MW/cm^2. Unfortunately, cavity losses still increased slowly, dropping the circulating power from 2.5 to 1.25 kW in roughly 2 h. No fluorescence was observed from the Ojai mirror. The higher finesse could be recovered by tilting the output mirror mount with the vacuum feedthrough screwdrivers enough to move the optic axis of the cavity 1–2 mm on the input mirror and 0.1–0.2 mm on the output mirror. Given the high circulating powers attainable, albeit temporarily, we used this configuration for the measurement presented here.

D. Build-up cavity lock

The cw dye laser is locked to the 1.6-kHz-wide resonance of the build-up cavity by the method of rf sideband locking [36], in which FM sidebands are impressed upon the carrier frequency of the incident laser beam at a spacing much greater than the bandwidth of the cavity. When tuned near resonance, the carrier is strongly absorbed by the cavity, while the sidebands are far from resonance and are entirely reflected. In detecting amplitude modulation (AM) in the light reflected from the cavity, the sidebands serve as a reference to determine the phase of the field in the resonant cavity. As with any oscillator, the phase of the cavity field near resonance is a monotonic function of the detuning of the driving field. On resonance, the field in the cavity is opposite in phase with the carrier reflected from the input mirror, resulting in no AM at the detector. As the laser deviates from resonance, the phase of the cavity field rotates to the new phase given by the laser detuning, producing amplitude modulation. An error signal is generated by demodulating the detected photocurrent in an rf mixer.

We briefly describe the particulars of our locking scheme. As shown in Fig. 5, the cw beam incident on the build-up cavity is passed through a telescope to match the incident transverse-mode parameters to the TEM_{00} mode of the cavity. The beam then passes through a special Faraday-rotating optical isolator we have constructed in collaboration with Optics for Research, Inc. The usual isolator material used in the visible spectrum is terbium-doped glass, which has a strong absorption near the Ps resonance line, making this material unacceptable for our application. Our isolator consists of an 8-mm rod of flint glass (Schott SF-57) inserted into a magnet assembly providing a 10-kG linear magnetic field. Absorption and deviation of the rotation angle from 45° result in an insertion loss of <0.3 dB, while the isolation exceeds -30 dB.

The isolator is required for two reasons. The dye laser must be isolated from the strong beam that is exactly retroreflected from the supercavity. Also, the rf locking scheme is extremely sensitive to interference caused by reflections from lenses and other optics. For this reason, the input and output mirrors are ground with a wedge of 3° and 0.5°, respectively. Isolating the build-up cavity from the mode-matching optics greatly reduces residual amplitude modulation that can interfere with the stable operation of the lock. An alternative technique, polarization isolation, requires that circularly polarized light be incident on the cavity, and is not an acceptable solution in our experiment since the counter-propagating photons of the same angular momentum do not excite the $1S$-$2S$ transition.

The beam then passes through a Gsanger PM-25 phase modulator driven at 4.0 MHz for 10% total sideband power. The relatively small modulation frequency is used to ensure complete separation of the error signal of adjacent transverse modes and to increase the size of the small error signal outside the central dispersive peak, improving the long-term stability of the lock. Instability in the laser lock was generally due to two sources: (i) sudden frequency disturbances in the dye laser caused by occasional bubbles and dust in the laser dye, and (ii) contamination of the error signal by residual AM. Since the error signal is very small outside the central dispersive peak, fluctuations in the error signal can prevent the laser lock from recovering from a large excursion. Residual AM of a nearly constant amplitude and phase is usually produced by the frequency modulator and produces a constant offset of the error signal that can be electronically corrected. AM introduced by interferences between

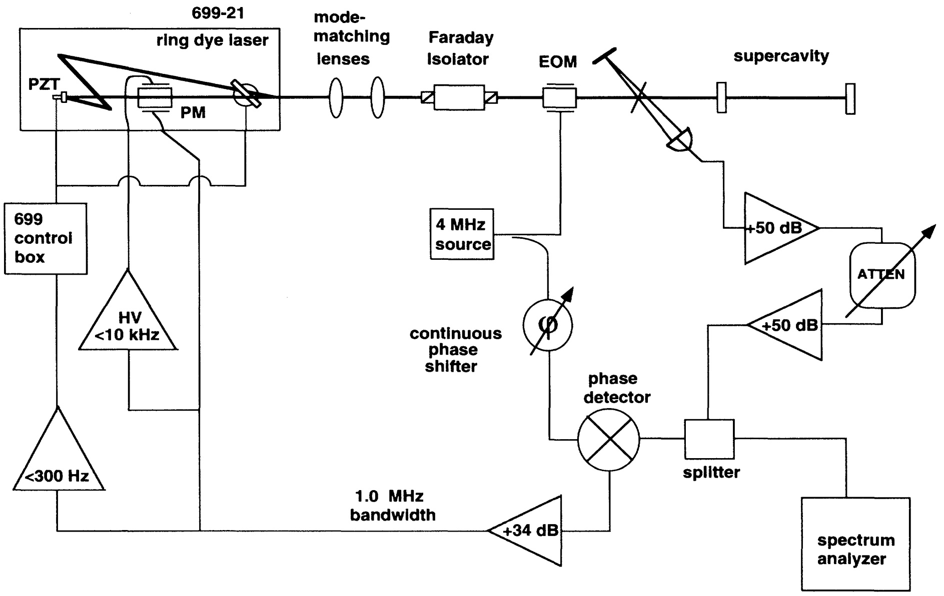

FIG. 5. Rough schematic of the laser stabilization electronics used to lock the Coherent 699-21 ring-dye laser to the ultrahigh-finesse build-up cavity. The modified Coherent 699-21 ring-dye laser contains an intracavity phase modulator to correct rapid phase fluctuations. The laser output is passed through a Faraday isolator and a frequency modulator to impose FM sidebands at ±4 MHz. A sample of the incident and reflected beams from the cavity is detected on a differential detector. Detected amplitude modulation at 4 MHz is amplified and subsequently demodulated using an rf phase detector. The phase signal is amplified and fed back to the intracavity phase modulator and, through the 699 control box, to the laser tuning elements.

various optical elements introduces fluctuations in the error signal at acoustic frequencies between 10 Hz and 1 kHz. In both of these cases, spurious AM appears on the incident as well as the reflected beam from the cavity.

A quartz plate near Brewster's angle is used to pick off a small fraction of the incident and reflected beams at the cavity input mirror to detect amplitude modulation. The two reflections are focused onto a pair of photodiodes connected in series to form a differential detector such that AM common to both incident and reflected beams is reduced by ~ 10 dB in the differential current signal. The rf photodiode signal is amplified by a Trontek ATC-50 low-noise amplifier (noise figure, $N = 1.1$ dB), a variable attenuator, and a second Trontek amplifier. Each of the detected beams is passed through a polarizer to eliminate AM due to birefringence in the frequency modulator. With careful alignment of the frequency-modulator polarization axis, the residual AM at 4 MHz could be reduced so that fluctuations in the error signal were less than 10% of the off-resonance error signal.

The amplified rf signal is demodulated at 4.0 MHz using a MiniCircuits RPD-1 phase detector. The local oscillator used for demodulation is derived from the driving field of the 4-MHz frequency modulator, and passed through a home-built 360° continuously variable phase shifter adjusted to maximize both the gain of the feedback loop and the laser power transmitted by the build-up cavity.

The phase detector output is amplified ($50\times$) using a Burr-Brown 3554 high-speed operational amplifier with a unity gain bandwidth of 2 GHz, providing what we will refer to as the error signal. Applied to one electrode of the intracavity phase modulator, the error signal produces high-frequency gain from 10 kHz to the unity gain frequency near 1 MHz. The sample error signal is further amplified by a high-voltage operational amplifier (BB 3584) capable of ± 150 V voltage swings, and applied to the other electrode of the phase modulator to provide higher gain at intermediate frequencies from 300 Hz to 10 kHz. Finally, a portion of the error signal is filtered with a 300-Hz cutoff and summed into test point TP2 of the Coherent 699-21 "differential amplifier" (board 1A9) to provide low-frequency gain using the intracavity Brewster plate. The gain of each branch of the servo loop is set as high as possible, while avoiding oscillation in the closed loop error signal.

The dye laser is simultaneously locked to its commercial reference cavity to facilitate recovery from occasional dye-jet disturbances (i.e., dust, bubbles). By summing the error signals from the 699 external reference cavity and the supercavity electronics the 699 locking electronics responds in such a way as to set the sum of these two error signals to zero. Thus, when the laser is locked to the build-up cavity, the build-up cavity error signal will not be zero, but will be offset from zero by a voltage proportional to the frequency difference between the lock points of the external reference cavity and the supercavity. The offset can be used to tune the external reference cavity frequency to coincide with the supercavity. We integrate the cavity error signal (20-Hz bandwidth) and apply the result to the external scan input of the 699 control box, resulting in linear tuning of the external reference cavity by the rotation of a Brewster's-angle galvo plate. The reference cavity tuning is thus fed back to actively track the tuning of the build-up cavity.

With proper care to eliminate residual AM in the incident laser beam, we were typically able to lock the laser continuously for more than an hour, sufficient for the half-hour runs we made in the experiment. To further test the quality of the laser lock, light transmitted by the build-up cavity was heterodyned with an acousto-optically frequency-shifted portion of the dye-laser output, and the beat signal was recorded on a digitizing oscilloscope. A fast Fourier transform revealed a broad noise pedestal centered under the carrier with a width of 800 kHz. Taking the ratio of the pedestal area to carrier area in the plot of the spectral intensity of the beat note, we found the fraction of power in the pedestal to be less than 5%.

E. Radio-frequency offset

A fraction of the cw dye-laser output is separated from the main beam and is tuned over a range of -100 to $+100$ MHz relative to the dye laser using acousto-optic modulators. The resulting beam is locked near the center of the e_3 reference line in Te_2 vapor by feedback to the acousto-optic tuning elements. The frequency of the cw dye laser relative to the reference line may then be measured as a rf frequency offset with a precision limited only by the frequency stability of the laser. (We have determined the stability of our stabilized dye laser relative to the Te_2 line center to be 200-kHz rms, measured with a 1-kHz bandwidth.) Although this precision allows us to generate a very linear frequency scan, the absolute frequency accuracy of this measurement is limited by offsets in the lock to the Te_2 line.

We now describe the scanning technique in more detail. Using a half-wave plate and a polarizing beamsplitter, 30 mW of the cw laser output is directed into a double-passed acousto-optic modulator (AOM), as shown in the "rf offset" box of Fig. 4. All of our AOM's are manufactured by Isomet, Inc., Model 120C. A zero-order quarter-wave plate in the output of the AOM is rotated to produce circularly polarized output. A lens (focal length, 31 cm) placed one focal length from the AOM, focuses the beam to a waist at a retroreflecting mirror, where an aperture passes only the -1 order of the AOM output. As the rf oscillator driving the AOM is tuned about its center frequency (120 MHz), the -1 order output of the AOM is deflected at different angles. However, with this optical arrangement, the -1 order is always exactly retroreflected onto itself at all tunings of the rf oscillator. The retroreflected beam passes again through the quarter-wave plate, and through the AOM, with its polarization 90° relative to incident beam. The -1 order of this second pass is transmitted through the polarizing beamsplitter with a net frequency offset of $-2\nu_1$ relative to the cw dye laser. The resulting beam is sent through another polarizing beamsplitter, and a second similar arrangement in which the AOM (AOM no. 2) is oriented to produce a $+1$-order diffraction. The retroreflected output beam from the second acousto-optic modulator is reflected by the second polarizing beamsplitter with a frequency offset of $\Delta\nu=2(\nu_2-\nu_1)$. Each AOM is independently tunable from 95 to 145 MHz with voltage-controlled rf oscillators (rf VCO). The laser power of the final frequency-shifted beam decreases to 50% of maximum at the ends of the tuning range.

The resulting beam, with a tuning range of -100 to $+100$ MHz relative to the cw dye laser, is sent to a frequency-modulated Te_2 saturated absorption spectrometer [37,38]. The spectrometer pump beam is modulated at 50 kHz using the -1 order of a 110-MHz AOM, resulting in a $+55$-MHz shift in the frequency at which the Te_2 line is observed. For heterodyne detection, the probe beam is phase modulated at 15 MHz with a modulation depth of $\Gamma=1$ using a home-built electro-optic modulator and impedance matching electronics. The detector output is demodulated in a MiniCircuits ZAD-1-1 rf mixer using a fraction ($+7$ dBm) of the 15-MHz power. A home-built 360° continuous phase shifter allows us to optimize the phase of the local oscillator input of the mixer. The demodulated 50 kHz signal is detected with a lock-in amplifier to obtain a dispersive line shape.

The probe beam has a small amount of residual amplitude modulation produced by the two double-passed AOM's. This AM was viewed on a rf spectrum analyzer and found to be at the frequencies $2\nu_1$, $2\nu_2$, and $2\nu_2-2\nu_1$. Under certain tuning conditions, $2\nu_2-2\nu_1=15.00\pm0.05$ MHz, in which case the residual AM is demodulated by the rf mixer to 50 kHz and is detected by the lock-in amplifier, resulting in large erroneous "blips" in the dispersive line shape. The residual AM at $2\nu_1$ and $2\nu_2-2\nu_1$ can be minimized by very careful alignment of the quarter-wave plate in the first leg of the double-passed AOM arrangement. The unwanted AM is additionally suppressed by splitting the probe beam into two parallel beams of equal intensity, which are incident on a differentially connected photodiode pair. Thus residual AM present on the probe beam is suppressed in the photodiode output. The pump beam overlaps with only one of these probe beams, producing saturated absorption-dependent AM in the output signal.

The dispersive Te_2 signal is integrated to generate a control voltage for the rf VCO of AOM no. 2. The output of the double-passed AOM arrangement is thus continuously frequency locked to the Te_2 line. We measure the rf driving frequency of the two tuning AOM's with a Phillips PM6665 frequency counter with a 100-ms counting gate. The offset between the cw dye-laser frequency and the Te_2 line is precisely determined at all times.

Tuning of the build-up cavity, shown schematically in Fig. 6, is effected as follows: the VCO control voltage for AOM no. 2 is differentially summed with a command voltage, the result is integrated, and followed by a high-voltage amplifier to drive the piezoelectric tuning elements (PZT's) of the build-up cavity. The cavity is tuned appropriately to force the VCO control voltage to equal the command voltage. Based on a linear approximation of the two VCO's, a computer calculates the command voltage and the VCO voltage of the AOM no. 1 required to achieve the desired frequency during a scan. Nonlinearities in the VCO responses result in an accuracy of ±1 MHz in the laser frequency offset. However, this is unimportant since the computer subsequently reads the frequency counters to record the true laser frequency offset.

F. Metrology — the tellurium spectrometer

To make our measurements insensitive to potential locking errors in the FM spectrometer, an independent Te_2 saturated absorption spectrometer [39,40] is used as the reference in our measurement. The saturation beam and the probe beam each had roughly 5(2)-mW laser power and a 1.0(2)-mm diam (to $1/e$ amplitude points). The initially 10-mW probe beam was passed through a 50% beamsplitter to give an intensity reference beam that was passed through the cell parallel to the probe beam. The difference in intensity of the probe beam and intensity reference beam was detected with a differential diode pair. The saturation beam used in the reference spectrometer is modulated using the -1 order of an acousto-optic modulator driven at 110.0 MHz. The resulting $+55.0$-MHz offset in the tellurium resonance frequency causes the line to appear near the peak of the Ps resonance during our experimental scans, in which both the tellurium and Ps signals are recorded. Our reference cell was purchased from Opthos Instruments within a year before our Ps measurement, and is 10 cm in length, compared to the 7.5-cm cell used in the McIntyre work [5]. To characterize the cell, the pressure dependence of the e_3 line center of the reference cell was studied and found to be -1.75 ± 0.30 MHz/torr, in disagreement with the -1.05 ± 0.32 MHz/torr measured by McIntyre. However, the erroneous cell temperature measurement reported in that work accounts for the discrepancy.

The body and stem temperature of both Te_2 cells were separately heated in an oven. The oven design has several important features. A copper block surrounding the cell stem ensures a uniform temperature and an accurate temperature reading. A quartz tube sleeve surrounding the cell body prevents contaminants from the heaters from condensing on and clouding the cell windows. Finally, the anti reflection-coated oven windows eliminate laser-beam fluctuations due to convection currents.

The thermocouples provide electronic feedback to stabilize the temperature to ±1 °C. At a body and stem temperature of 549(5) and 485(5) °C, respectively, we measured the linear absorption on the Doppler-broadened peak of the e_3 line to be 30(3)%. When scaled to a 7.5-cm cell this is equivalent to 24(2)%, the same as that reported by McIntyre *et al.* for a temperature of 513(5) °C. Based on linear absorption measurements of a Doppler-broadened line 9 GHz below the frequency of the b_2 line, Barwood *et al.* [52] also report a discrepancy in the McIntyre temperature reading. They find that the 23(2)% linear absorption reported by McIntyre for this line is consistent with a stem temperature of 480 °C, in agreement with our temperature estimate.

Seven months after our positronium runs had ended, the reference cell used in our Ps 1*S*-2*S* measurement was brought to the laboratory of Professor Hänsch at the Max Planck Institut für Quantenoptik in Garching, Germany, for calibration. The oven and cell were never disassembled and were at room temperature in the intervening period. They were transported intact as used in our Ps measurement. The temperature controller used in our measurement was also brought to Münich and used during the calibration.

We calibrated the cell relative to the hydrogen 1S-2S ($F=1$ to 1) two-photon transition frequency which was recently measured by the Hänsch group to be $\nu_{H/2}=1\,233\,030\,551.235(021)$ MHz [53]. They use a dye laser at 486 nm, nearly identical to one described in this paper, locked to a temperature stabilized, vibration isolated, high-finesse reference cavity. The frequency of the hydrogen 1S-2S transition is compared (over ~6400 reference cavity modes) to the seventh harmonic of a methane-stabilized helium-neon laser (HeNe-CH_4), generated with a phase-locked frequency chain. The free spectral range (FSR) of the reference cavity has been determined to be $\nu_{\mathrm{FSR}}=332\,383\,360.5\pm1.0$ Hz using a second dye laser passed through an 84-GHz electro-optic modulator. The HeNe-CH_4 secondary standard was calibrated at the Physikalish-Techniche Bundesanstalt (PTB) in Braunschweig by comparison with the Cs atomic clock using the PTB frequency chain.

For the hydrogen measurement, a fraction of the dye-laser output is double passed through the +1 order of an AOM, and mode matched into the TEM_{00} mode of the reference cavity. When thus locked to the cavity, the laser is tuned by varying the rf frequency of the AOM driver, giving a scan range of 20 MHz. The majority of the dye-laser output is frequency doubled using a beta-barium-borate crystal in a resonant build-up cavity, and the resulting 243-nm radiation is used to excite a 77-K beam of hydrogen atoms to the 2S state. The excited-state atoms are counted by field quenching and detection of the emitted Lyman-α fluorescence.

We accomplished the calibration of the Te_2 line as follows. We tuned the dye laser near the hydrogen resonance as identified by the i_2 component of Ref. [54] in

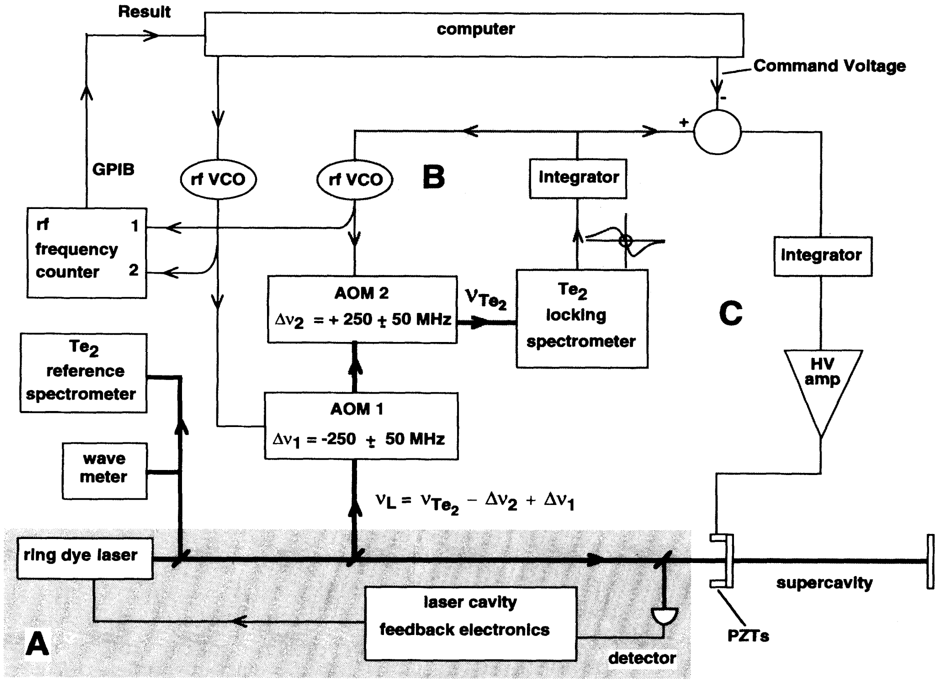

FIG. 6. Three main feedback loops operate simultaneously to allow highly linear frequency scans over a 200-MHz range. Loop A locks the ring-dye-laser frequency to the 2-kHz linewidth of the build-up cavity. An rf sideband lock technique [36] provides a roughly 1-MHz servo bandwidth to modulate an intracavity phase modulator in the ring-dye laser. The result is a 100-Hz stability of the dye laser relative to the chosen build-up cavity resonance. Loop B locks the laser output of the acousto-optic modulator AOM no. 2 to the correct frequency such that the output of the locking spectrometer is held at 0 V. The integrated spectrometer output is used to control a radio-frequency (rf) voltage-controlled oscillator (rf VCO no. 2), which drives AOM no. 2. When the frequency-shifted beam reaches the correct frequency, the spectrometer output voltage is zero, and the integrator holds the control voltage constant. As the build-up cavity is piezoelectrically tuned, the dye-laser frequency follows due to lock A and the control voltage and modulation frequency of AOM no. 2 follow due to lock B. Lock C controls the high voltage on the build-up cavity piezoelectric tuning elements (PZT's) to force the control voltage V_{RF2} of rf VCO no. 2 to a preset value. The difference of V_{RF2} and a command voltage V_{com} provides an error signal which is integrated, and amplified sufficiently to drive the PZT's, forcing the error signal to zero. The frequency of the cavity resonance is then locked to the tellurium line with an offset determined by the command voltage V_{com} and a RMS stability of ±0.2 MHz determined by the voltage-controlled oscillator and cavity vibrations. By varying the driving frequency of AOM no. 1, the range of our frequency scan is extended by a factor of 2.

Te_2 vapor. The dye laser was then locked to an appropriate resonance of the stable reference cavity so that the hydrogen resonance appeared within the tuning range of the AOM. The 40-kHz-wide hydrogen resonance was recorded by computer as a function of the AOM frequency. The dye laser was then tuned near the e_3 line in Te_2 where the laser was again locked to a mode of the stable reference cavity. The e_3 line was then scanned several times and recorded as a function of the AOM frequency.

Scans were made at several temperatures of the Te_2 cell stem, while holding the cell body temperature constant at 549(5) °C. The linear absorption on the Doppler-broadened peak was determined to be 50(5)% at a temperature reading of 517(5)°C, in agreement with a value previously measured for this cell at AT&T Bell Laboratories. When we finished the measurements of the Te_2 cell, 2.5 h had elapsed since our scan of the hydrogen line, so we repeated that observation to find that the cavity had drifted only 30 kHz relative to half the hydrogen transition frequency. Since the e_3 positronium reference line sits on the side of a smaller, much broader line, all of the tellurium resonances were then fit to a model line shape given as the sum of two Lorentzian peaks, with no dispersively asymmetric term:

$$y=A_0+A_1\frac{\gamma_1^2}{\gamma_1^2+(f-f_1)}+A_2\frac{\gamma_2^2}{\gamma_2^2+(f-f_2)}\ , \tag{6}$$

where $A_2/A_1=0.12$ is the measured amplitude ratio of the smaller companion line to the e_3 line, and $f_1-f_2=175$ MHz is the measured frequency separation between the components. The width of the smaller component was measured to be $\gamma_2=175$ MHz. Any dc offsets were accounted for by the coefficient A_0. Note that the AOM is double passed, so a 1-MHz change in the AOM frequency produces a 2-MHz change in the actual laser frequency. All of the above quantities are expressed in laser frequency, not AOM frequency. The unconstrained fit parameters were A_0, A_1, γ_1, and f_1. The value of f_1 for the same oven temperatures and laser power as that used in the Ps measurement was $2\nu_2=491.22$ MHz, corresponding to an AOM frequency of $\nu_2=245.61$ MHz.

The center of the hydrogen resonance was observed at an AOM frequency of $\nu_1=155.47$ MHz. The laser frequency ν_{obs} at the center of the observed e_3 resonance is therefore given by

$$\nu_{\text{obs}}+2\nu_2=\tfrac{1}{2}\nu_{H/2}+2\nu_1+868\nu_{\text{FSR}}\ . \tag{7}$$

A previous calibration of the e_3 line [51] allowed us to determine that, for the hydrogen scan, the laser was locked to a mode ($M1$) 868 free spectral ranges lower in frequency than mode $M2$ used for the tellurium scans. The pump beam of the saturation spectrometer used in this calibration was derived from the -1 order diffraction of an AOM, used as a chopper for lock-in detection. The AOM was driven by a frequency synthesizer set at 120 MHz, producing a $+60$-MHz shift in the laser frequency at which the resonance was observed. The hydrogen $1S$-$2S$ transition frequency and the tellurium e_3 line are shown relative to the modes of the stable reference cavity in Fig. 7.

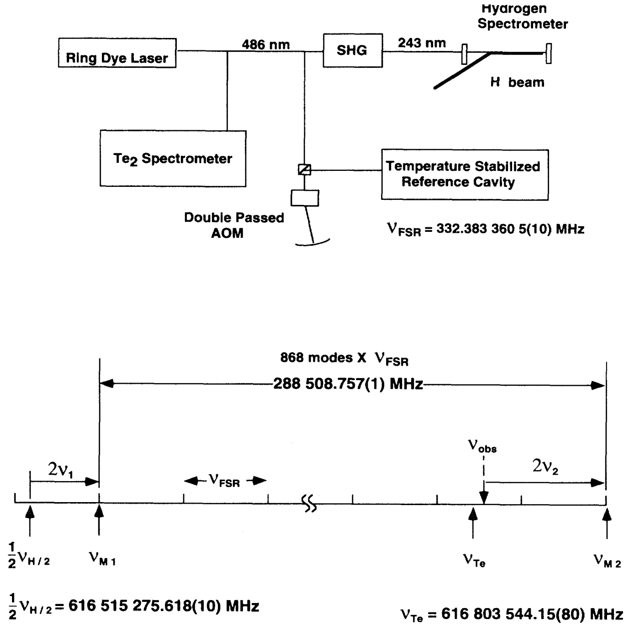

FIG. 7. Schematic of the apparatus and the mode structure of the stable reference cavity used in calibrating our tellurium reference cell. The calibration was carried out in two steps. First, the frequency ν_{M1} of a mode ($M1$) was measured as an acousto-optic frequency offset relative to half of the hydrogen $1S$-$2S$ ($F=1{:}1$) transition frequency. Similarly, the frequency of the positronium reference line was determined relative to another, nearby mode $M2$. Our knowledge of the free spectral range (ν_{FSR}) to an accuracy of 1.0 Hz permitted the frequency comparison over 868 cavity modes, less than 300 GHz.

Therefore, the frequency of the e_3 line of our cell at a stem temperature of 485 °C, was found to be $\nu_{\text{Te}}=616\,803\,544.4\pm0.6$ MHz. Contributions to the quoted uncertainty are detailed in Table II. We measure a -200-kHz change in the Te_2 line center when the total laser intensity of the pump and probe beams is increased from 2.0 to 6.0 W/cm^2. We include this power shift in our uncertainty estimate since the cw laser power was varied over a comparable range during our Ps measurements. Our measurement reproduces the tellurium vapor pressure condition in the McIntyre work [51], which reports a frequency for the e_3 line of $616\,803\,545.31\pm0.57$ MHz, 0.9 MHz higher than our measurement of the frequency of our cell. In addition, Barwood *et al.* [52], and Gillaspy and Sansonetti [55] both report calibrations of the e_3 line that, after scaling to a cell pressure corresponding to 485 °C, give nearly equal values of 616 803 545.5 MHz with uncertainties of 0.47 and 0.9 MHz, respectively.

All of the previous calibrations relied on interferometric comparisons of the 486-nm laser with the internationally accepted I_2 stabilized HeNe visible frequency standard at 633 nm. Although the phase-shift problems inherent in interferometric frequency determinations are expected to be small (<300 kHz), to our knowledge ours is the first Te_2 calibration based on direct

TABLE II. Measurement uncertainties for tellurium cell calibration.

Source of uncertainty	Standard deviation (MHz)
Half of hydrogen 1*S*-2*S* transition frequency	0.01
Computer fit (systematic error)	0.1
Measurement repeatability	0.1
Linear absorption reproducibility from Ps measurement	0.1
Laser power shift	0.2
Pressure shift reproducibility	0.5
Total	0.6

frequency comparison, thus avoiding the phase-shift problem entirely. The National Institute of Standards and Technology (NIST) has recently lowered the frequency [56] of the I_2 standard by 100 kHz to bring it into line with the cesium standard, thus reducing the discrepancy between our calibration and the McIntyre calibration to roughly 0.75 MHz, comparable to the peak cell-to-cell variation reported by Barwood *et al.* with a sample size of four cells.

It is possible that the frequency of our cell changed between the Ps measurements and our calibration due to air leakage through microcracks in the quartz tubing. However, the linewidth of the e_3 line measured at the time of the Ps measurement and at the time of the calibration were 14.0(5) and 14.5(5) MHz, respectively, both in agreement with the McIntyre result of 14.0(5) MHz. In addition, over the two days on which we calibrated the cell, it was kept at 500 °C, and there was no discernible change in the linewidth or line center of the e_3 line during that time. Since the pressure shift is roughly the same or less than the pressure broadening for most possible contaminants [56], we take the uncertainty in the pressure shift to be equal to the difference between the linewidth measured at the time of the Ps measurement and our Te_2 calibration. The result of our calibration is therefore entered in Table II with an uncertainty of ±0.6 MHz.

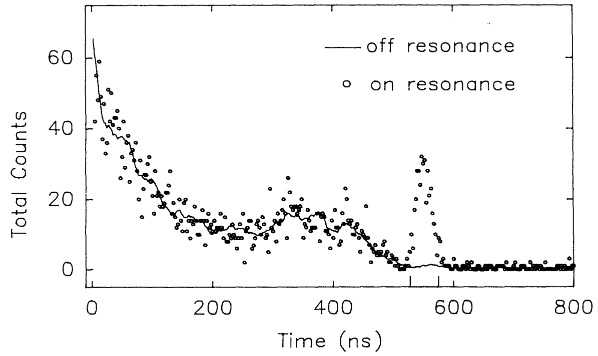

FIG. 8. Time spectra both on and off the Ps resonance. The background signal shown is averaged in ten bin intervals. The excess counts due to photoionization of 2*S* positronium are clearly visible between 530 and 575 ns.

G. Experimental procedure

We took 15 resonances at an Al target temperature of 576 K and 7 resonances at a target temperature of 235 K. The laser frequency was scanned in 5-MHz steps for 3.3-s intervals (100 e^+ pulses). The intensity of the incident positron beam was monitored by a NaI scintillator and a photomultiplier tube to observe the burst of γ radiation produced by annihilation of the incident positrons at the Al target. The NaI pulses were stretched by a sample-and-hold and integrated over the 3.3-s interval (100 pulses) via a voltage-to-frequency converter and a counter that was subsequently read by computer. The transmitted laser power through the build-up cavity was continuously monitored by photodiode and recorded by the computer at each 3.3-s interval. We calibrated the recorded voltage to reflect an absolute power in the build-up cavity as follows: The transmission of the output mirror was measured to be (1.86±0.02) ppm using a recently calibrated HP 8153 A lightwave multimeter with an HP 81520 power meter head, which is specified to be calibrated to $\sigma = 1.3\%$ accuracy at 486 nm with a linearity of $\sigma = 0.05$ dB over the range of +10 to −80 dBm. The response of the photodiode and associated optics to the laser power transmitted by the build-up cavity was also measured over the range of −10 to +10 dBm and found to be linear to within the 3% rms statistical error of the measurements. The measured conversion factor of photodiode reading to build-up cavity power is 761.5±20 W/V.

At the end of each 3.3-s frequency interval, a sequence of 100 time spectra were down-loaded from the LeCroy oscilloscope to the computer. Figure 8 shows the time spectra both on and off the Ps resonance, with the excess counts due to photoionization of 2*S* positronium clearly visible between 530 and 575 ns.

In Fig. 9 we show the results of a sequence of repeated laser-frequency sweeps, each scanning from −100 to +100 MHz in 5-MHz intervals, and each taking roughly 3.5 min. The top trace shows the number of counts detected in the time interval between 530 and 575 ns of the time spectrum shown in Fig. 8. Each resonance in the top trace of Fig. 9 shows the cumulative number of counts including all the earlier scans shown. The middle trace shows the Te_2 reference line acquired simultaneously with the Ps resonance. The lower trace shows the average positron beam strength measured during the

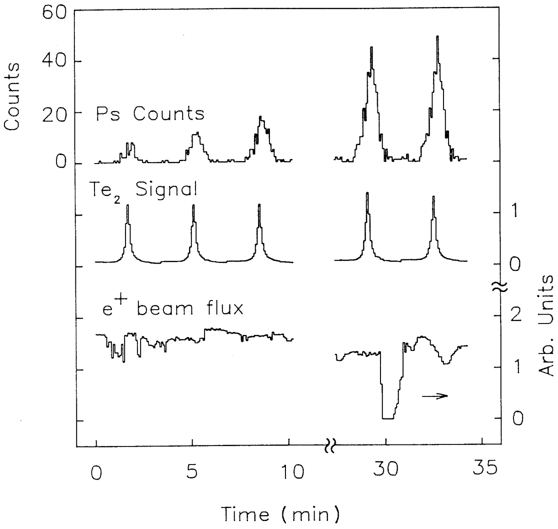

FIG. 9. The results of a sequence of repeated laser frequency sweeps, each scanning from -100 to $+100$ MHz in 5-MHz intervals, and each taking roughly 3.5 min. The top trace shows the number of counts detected in the 45-ns interval of the time spectrum shown in Fig. 8. Each resonance in the top trace shows the cumulative number of counts including all the earlier scans shown. The middle trace shows the tellurium line e_3 acquired simultaneously with the positronium resonance. The lower trace shows the positron beam strength measured during each 3.3-s frequency step.

3.3-s frequency step. Scans were taken at several time delays of the photoionization pulse and at several settings of the build-up cavity power, allowing us to understand and eliminate the systematic effects in determining the positronium $1S$-$2S$ line center relative to the Te$_2$ reference line. The major systematic effects are (i) the second-order Doppler shift due to the motion of the Ps atom in the laser reference frame, and (ii) the ac Stark effect due to the nearly saturating cw laser beam. For the majority of the data taken, both systematic corrections are less than 20 MHz.

III. MODEL LINE-SHAPE CALCULATION

There are a number of strategies one may adopt in determining the positronium line center from the measured resonances. One may simply fit the experimental resonances to some simple model function and extrapolate the frequencies of the resonance peaks to zero laser power and zero Ps kinetic energy. This was the strategy used in the previous positronium $1S$-$2S$ measurement [2], where the resonance line was modeled as a Lorentzian function. The significant asymmetry of the resonances we report here, resulting from the dynamics of the nonlinear transition [27] and from the second-order Doppler shift, indicate that more information is contained in the data than may be extracted using such a simple model. Additionally, the complicated dependence of the resonance peaks on the laser beam power and the YAG pulse delay make extrapolating to the true line center unreliable. An understanding of the experimental geometry, positronium velocity distribution, laser beam power, and beam diameter, coupled with detailed modeling of the line shape, places constraints on the determination of the positronium line center not possible with simple extrapolation.

We have therefore developed a Monte Carlo model of our experimental geometry allowing us to integrate the excitation and photoionization probabilities for a large number of positronium trajectories chosen randomly from an initial beam-Maxwellian distribution at the temperature of the Al sample. For each classical atomic trajectory, the model line shape is determined, including the ac Stark effect and the photoionization and annihilation rates, and the resulting transition probabilities are summed to obtain a model of the observed resonances.

A. Positronium trajectories

The positronium velocities are assumed to have a beam Maxwellian profile based on measurements by Mills *et al.* [49]. The velocity distributions perpendicular and parallel to the target surface are given by

$$\begin{aligned}\frac{\partial n}{\partial v_\perp}&=2N_0\frac{v_\perp}{\alpha}\exp\left[\frac{v_\perp^2}{\alpha^2}\right],\\ \frac{\partial n}{\partial v_\parallel}&=2N_0\frac{v_\parallel}{\alpha}\exp\left[\frac{v_\parallel^2}{\alpha^2}\right],\end{aligned}\tag{8}$$

where $\alpha^2=2k_BT/M_{\text{Ps}}$, k_B is Boltzmann's constant, T is the temperature of the Al target, and M_{Ps} is the mass of the Ps atom. The distributions in Eq. (8) are consistent with a Knudsen's law distribution in the polar angle from the normal to the surface (z axis). The choice of variables used allows for easy integration to obtain an appropriately distributed ensemble of velocities in terms of a uniform deviate (Θ): $v_i=-\alpha\ln\Theta$. The third dimension of the atomic trajectory, the azimuthal angle, is chosen with a uniform distribution.

In our model the source positions of the ensemble of trajectories are uniformly distributed in a 10×6-mm^2 rectangular area on the surface of the Al target (x-y plane) with the long axis along the cw laser beam. The start time of the trajectory is chosen with a triangular distribution with a full width at half maximum (FWHM) of 25 ns to account for the nonzero temporal width of the incident positron beam. A trajectory is thus determined by a set of six random numbers. Unfortunately, most commercial random number generators have sequential correlations. We use a generator of uniform deviates that is free of such correlations [57].

The cw excitation beam is assumed to be parallel to the plane of the Ps source, and of a constant radius calculated to be $w=0.31(1)$ mm at the position of the target 25 cm from the cavity waist. The YAG pulse is sent through the photoionization region in eight passes, where pairs of passes are nearly overlapped spatially and temporally. There are effectively four passes with a 6-ns delay; the model photoionization region is thus sampled four times at 6-ns intervals. In aligning the apparatus, we attempted to position the 6-mm-diam YAG beams as close to the target as possible, while avoiding visible clipping of the retroreflected beams. We estimate that the effective edge of the photoionization region was between 1 and 2 mm from the target, with a 68% confidence interval. The YAG beam has an elliptical shape on each of its four passes through the photoionization region producing four cylindrical regions (of elliptical cross section) of photoionization. The major diameter (b) of the first pass of the YAG beam was measured from the spot of scattered light on the fold mirror to be 6.0 ± 0.5 mm. The minor diameter (a) was constrained to be less than 6.5(5) mm by the spacing of the fold mirrors. The spots of light on the YAG retroreflecting mirror were clearly visible on the monitor screen of a video camera used to align the YAG beams, and a trace of their position and approximate shape was made on the screen. The minor diameters of the three subsequent passes were measured to be 1.19, 1.19, and 1.38 times that of the first pass. The ellipticity (b/a) of the four passes of the YAG beam was also measured using the camera to be 1.2, 1.3, 1.3, and 1.4 with an uncertainty of ±0.2 for each.

A sample of 10^5 trajectories is generated, and for each trajectory that is within the model photoionization region at the time of the YAG pulse, several parameters required for calculating the atomic line shapes are determined: (i) the distance of closest approach of the trajectory to the excitation beam yields the peak intensity seen by the atom relative to peak laser beam intensity, (ii) the Gaussian pulse width of the excitation field as seen by the moving atom, (iii) the second-order Doppler shift experienced by the atom due to relativistic time dilation, and (iv) the time required for the atom to reach the point of closest approach to the cw laser beam, allowing us to account for decay of the positronium ground state during the atomic trajectory.

A histogram of trajectories using these four line-shape parameters was generated at each of five YAG delay times: 50, 80, 120, 160, and 200 ns. As can be seen in Fig. 10, the last three parameters, (b) pulse width, (c) second-order Doppler shift, and (d) the time spent in the ground state, are all correlated with the YAG timing and thus with the speed of the atom. It is therefore necessary to generate a three-dimensional histogram with one of these parameters along each axis. A representative range of each parameter is chosen and divided into evenly spaced bins. For the laser pulse width the interval was 0–25 ns divided into 100 bins, second-order Doppler shift the interval was 0–500 MHz divided into 100 bins, and for the time to closest approach, the interval was 0–250 ns divided into 25 bins. To generate the histogram, the bin corresponding to the triplet of correlated parameters is incremented by 1.

The distance of closest approach of the atom to the cw laser beam center is independent of atomic speed, as demonstrated in Fig. 10(a), showing the histogram of the peak intensity parameter at a YAG delay of 50 and 200 ns. This lack of correlation with speed allows us to integrate this parameter separately, resulting in much faster calculations.

Aside from a shift in the center of the atomic resonance by the second-order Doppler shift, the shape of the resonance associated with each atomic trajectory is deter-

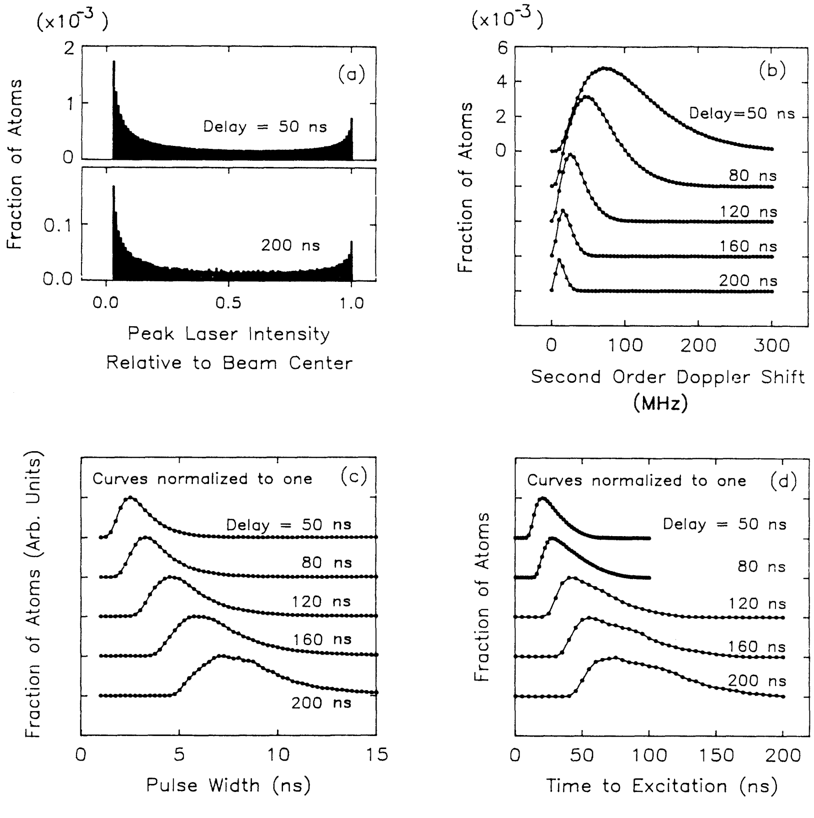

FIG. 10. Histograms of the four parameters required for the model line-shape calculations. (a) Peak intensity (relative to the intensity at beam center) seen by an ensemble of 10^5 atoms for a photoionization (YAG) pulse delay of 50 and 200 ns. The distributions are clearly independent of the delay and, thus, the positronium velocity. The lack of correlation between velocity and peak intensity allows us to include a smaller sample of atoms to achieve the same model line-shape statistics, significantly speeding up the calculation. (b) The distribution of second-order Doppler shifts of the same ensemble of 10^5 atoms at various YAG delays. Note that as the YAG delay becomes longer, the distribution becomes narrower as expected. (c) The distribution of effective excitation pulse widths as the atoms pass through the cw laser beam. The pulse widths become longer at longer delays. (d) The distribution in the time required for the atom to travel from the source to the cw laser beam is used to include the effects of ground-state decay on the net excitation and detection probability.

mined solely by the peak intensity and the pulse width. The "travel time" of the ground-state atom determines only the probability that an atom will annihilate before reaching the excitation beam. For each pairwise combination of the peak intensity parameter and the pulse-width parameter, the two-photon line shape is calculated as detailed below, in 5-MHz intervals, generating a two-dimensional table of line shapes.

B. Atomic amplitude equations

To generate the lookup table of line shapes, we solve numerically the equations for the interaction picture atomic amplitude coefficients. These were obtained from the results of a conventional second-order, semiclassical calculation of the two-photon transition, as discussed in detail by Beausoleil [58]. We present here only a brief summary of those results. In the electric-dipole approximation the interaction Hamiltonian is

$$V=-ea_0\mathbf{d}\cdot\mathbf{E}(\mathbf{r},t)\ , \tag{9}$$

where $\mathbf{E}(\mathbf{r},t)$ is the total classical electric field at the position of the atom, and $-ea_0\mathbf{d}$ is the electric-dipole operator. We write the total electric field as the sum of two counter-propagating fields with complex vector amplitudes $\mathbf{E}_1(\mathbf{r},t)$ and $\mathbf{E}_2(\mathbf{r},t)$, and a common carrier frequency (ω).

$$\mathbf{E}(\mathbf{r},t)=\tfrac{1}{2}\mathbf{E}_1(\mathbf{r},t)\exp(-i\omega t)+\tfrac{1}{2}\mathbf{E}_2(\mathbf{r},t)\exp(-i\omega t)+\text{c.c.} \tag{10}$$

In the interaction representation, the equations for the atomic probability amplitudes for the excited state, $C_a(t)$, and for the ground state $C_b(t)$, may be written containing no optical frequencies:

$$\begin{aligned}\dot{C}_a&=-i\Delta\omega_a(t)C_a-\frac{i}{\hbar}V_{ab}(t)\exp(-i\Omega t)C_b\ ,\\ \dot{C}_b&=-i\Delta\omega_b(t)C_b-\frac{i}{\hbar}V_{ba}(t)\exp(-i\Omega t)C_a\ ,\end{aligned} \tag{11}$$

where the detuning in the full interval is $\Omega=\omega_{ab}-2\omega+\omega_D$. We make the following definitions: $\omega_{ab}=\omega_a-\omega_b$ is the angular frequency difference between the Bohr frequencies of state $|a\rangle$ and state $|b\rangle$, ω is the angular frequency of the laser, and the second-order Doppler shift is $\omega_D=\omega_{ab}(v^2/c^2)/2$. We also define the radial matrix element between the state $|a\rangle$ and an intermediate state $|n\rangle$ as $\mathbf{d}_{an}=\langle a|\mathbf{d}|n\rangle$. The complex energy eigenvalue of the excited state in the presence of the field is $\hbar\Delta\omega_a(t)$, where

$$\Delta\omega_a(t)=-\frac{\Gamma_a}{2}+\left[\frac{ea_0}{2\hbar}\right]^2\sum_n\left[\frac{|\mathbf{d}_{an}\cdot[\mathbf{E}_1^*(\mathbf{r},t)+\mathbf{E}_2^*(\mathbf{r},t)]|^2}{\omega_{an}+\omega}+\frac{|\mathbf{d}_{an}\cdot[\mathbf{E}_1(\mathbf{r},t)+\mathbf{E}_2(\mathbf{r},t)]|^2}{\omega_{an}-\omega}\right] \tag{12}$$

with a similar expression for $\Delta\omega_b(t)$. The interaction potential may be written as

$$\frac{V_{ab}(t)}{\hbar}=\left[\frac{ea_0}{2\hbar}\right]^2\sum_n\frac{\mathbf{d}_{an}\cdot[\mathbf{E}_1(\mathbf{r},t)+\mathbf{E}_2(\mathbf{r},t)]\mathbf{d}_{nb}\cdot[\mathbf{E}_1(\mathbf{r},t)+\mathbf{E}_2(\mathbf{r},t)]}{\omega_{bn}+\omega}\ . \tag{13}$$

With these equations in hand, it remains only to determine the electric field of the laser.

C. Laser field

We assume the following separable form for the field amplitudes:

$$\mathbf{E}_j(\mathbf{r},t)=\hat{\xi}_jE_j(t)U_j(\mathbf{r})\exp(-i\mathbf{k}_j\cdot\mathbf{r}),\quad j=1,2\ , \tag{14}$$

where ξ is a complex unit polarization vector, $E_j(t)$ is a complex scalar with units of electric field, and $U_j(\mathbf{r})$ is the unitless complex spatial envelope of the laser field. If $\mathbf{E}_1$ and $\mathbf{E}_2$ are nearly counter-propagating waves, as in a build-up cavity, an atom with a component of its velocity collinear with the optical propagation axis will experience these fields with nearly opposite Doppler shifts. Thus only the two terms in the interaction potential involving products of E_1 and E_2 will contribute to the Doppler-free transition. We neglect the terms involving the squares of $E_1(t)$ and $E_2(t)$ as these terms contribute only to a Doppler-broadened line, which for thermal positronium is hundreds of gigahertz wide, and is thus of no consequence in determining our experimental line shape. The standing-wave nature of the laser beam does not appear in the interaction potential for the Doppler-free two-photon transition; only the temporal and spatial envelope quantities remain.

The time dependence of the laser field as seen by the atom is assumed to be due solely to the motion of the atom through the laser beam, and will depend on the spatial properties of the laser beam, which includes a transverse and longitudinally varying intensity envelope, and curved wave fronts. Because of the nondegeneracy of the transverse modes in our build-up cavity, we are able to excite primarily the TEM_{00} mode. To the extent that we may neglect thermal distortion of the cavity mirrors, the spatial dependence of the fields at the position of the atom $\mathbf{r}(t)=(r,\theta,z)$ is assumed to have the following form in the cylindrical coordinates of the laser beam [59]. The wave propagating in the $+z$ direction is

$$U_1(r,\theta,z)=\frac{w_0}{w(z)}\exp\left[-ikz+i\Psi(z)-\frac{r^2}{w^2(z)}-i\frac{kr^2}{2R(z)}\right], \quad (15)$$

and in the z direction is

$$U_2(r,\theta,z)=\frac{w_0}{w(z)}\exp\left[+ikz-i\Psi(z)-\frac{r^2}{w^2(z)}+i\frac{kr^2}{2R(z)}\right], \quad (16)$$

where these two fields have been written out explicitly to clarify the signs of the various phase terms. In terms of the Rayleigh range $z_R=\pi w_0^2/\lambda$, the beam radius as a function of z is

$$w(z)=w_0\left[1+\frac{z^2}{z_R^2}\right]^{1/2}, \quad (17)$$

the wave-front radius of curvature is

$$R(z)=z+\frac{z_R^2}{z}, \quad (18)$$

and the Guoy phase shift is

$$\Psi(z)=\tan^{-1}\left[\frac{z}{z_R}\right]. \quad (19)$$

With the extremely good approximation that E_1 is equal to E_2 in our high-finesse cavity, we verify that these fields give the expected standing-wave intensity distribution:

$$\begin{aligned}I(r,\theta,z)&\propto|U_1(\mathbf{r})+U_2(\mathbf{r})|^2\\&=4\frac{w_0^2}{w^2(z)}\exp\left[-\frac{2r^2}{w^2(z)}\right]\\&\quad\times\cos^2\left[kz\left[1+\frac{1}{2}\frac{r^2}{z^2+z_R^2}\right]-\Psi(z)\right]. \quad (20)\end{aligned}$$

The first term in the $\cos^2$ function results from the curvature of the standing-wave fronts. The second term results because larger transverse field derivatives near the beam waist increase the phase velocity, and thus, the distance between standing waves.

The two-photon interaction potential has the following form for these fields:

$$\frac{V_{ab}(t)}{\hbar}\propto U_1(\mathbf{r})U_2(\mathbf{r})=\frac{w_0^2}{w^2(z)}\exp\left[-\frac{2r^2}{w^2(z)}\right]. \quad (21)$$

It is clear that the wave-front curvature of the cw beam has no effect on the Doppler-free two-photon interaction as long as the counter-propagating beams have matched phase fronts, a condition guaranteed in a build-up cavity. The intuitive argument for this result is that the absorption of photons from the counter-propagating beams must occur with a relative delay of no more than the inverse of the intermediate state detuning, which is an optical frequency for Ps. Thus the transition line shape is sensitive only to local mismatch of the two laser waves, not the global curvature associated with a focusing beam. This agrees with the result found by inserting the given fields into the two-photon shape formulated by Bordé [60].

The positronium source in our experiment was placed 25 cm from the beam waist of the build-up cavity to take advantage of the slightly larger beam, reducing the Gaussian, transit-time-broadened component of the line shape. At this position, the wave-front radius of curvature is 1.25 m, however we neglect this curvature by the arguments given above. In addition, since the positronium source covers roughly 1% of the confocal length of the excitation beam, we neglect the variation of the beam radius along the axis of the beam.

The sum of matrix elements shown in Eq. (13) has been calculated for hydrogen by a number of authors [58,61]. For linearly polarized light, the interaction potential in positronium used in our model is eight times that of hydrogen:

$$\frac{V_{ab}(t)}{\hbar}=37.3\ \mathrm{cm^2/J}\times\bar{I}(\mathbf{r})\ \mathrm{W/cm^2}, \quad (22)$$

where

$$\begin{aligned}\bar{I}(\mathbf{r})&=\frac{1}{2\eta}E_1(t)E_2(t)U_1(\mathbf{r})U_2(\mathbf{r})\\&=\frac{2P_0}{\pi w^2(z)}\exp\left[-\frac{2r^2}{w^2(z)}\right], \quad (23)\end{aligned}$$

$\eta=377\ \Omega$ is the impedance of free space, and P_0 is the circulating power in the cavity.

The second line in Eq. (12) gives the Stark shift of the state under consideration. An atom moving in the standing wave discussed above traverses many wave fronts on average, and experiences a rapid sinusoidal variation in its Stark shift. It is not necessary to integrate Eq. (12) on this time scale, since this variation is rapid compared to the Rabi frequency.

The sum in Eq. (12) over all discrete and continuum P states has been previously considered for the hydrogen $1S$ and $2S$ states [58,62,63]. Since the ac Stark shift is proportional to the cube of the Rydberg constant, for light near the $1S$-$2S$ transition frequency, the result for the shift in the full $1S$-$2S$ interval in positronium is higher by a factor of 8 than in hydrogen:

$$\Delta\nu_{\mathrm{Stark}}=13.3\ \mathrm{cm^2/J}\times2\bar{I}(\mathbf{r})\ \mathrm{W/cm^2}. \quad (24)$$

Decay of the ground and excited states to all other states by annihilation and photoionization to the continuum is included in the Γ_a and Γ_b terms. The cross section for photoionization of Ps from the $2S$ state by 486-nm radiation is calculated to be $\sigma_{\mathrm{II}}=2.47\times10^{-17}\ \mathrm{cm^2}$ giving a photoionization rate [64] also eight times that of hydrogen:

$$\Gamma_{\mathrm{II}}=60.5\ \mathrm{cm^2/J}\times2\bar{I}(\mathbf{r})\ \mathrm{W/cm^2}. \quad (25)$$

Annihilation and radiative decay of the $2\,^3S_1$ state are neglected. The annihilation rate of the ground state is $\Gamma_{b\gamma}=7.14\times10^6\ \mathrm{s^{-1}}$. Thus,

$$\Delta\omega_a(t) = -\frac{i}{2}(\Gamma_{a\gamma}+\Gamma_{\mathrm{PI}})+2\pi\Delta\nu_{\mathrm{Stark}} \tag{26}$$

and

$$\Delta\omega_b(t) = -\frac{i}{2}\Gamma_{b\gamma} \tag{27}$$

are the complete complex eigenvalues used in the model.

D. Model results

Each four-component vector specifying a position in the three-dimensional trajectory histogram and a position in the intensity histogram is associated with a unique line shape. The next step in the procedure is to sum together all of these line shapes with an appropriate weight. For each occupied entry in the three-dimensional trajectory histogram, the following procedure is iterated for all elements of the intensity histogram: (i) the tabulated line shape corresponding to the given values of intensity and pulse width is accessed, (ii) shifted by the given second-order Doppler shift, (iii) weighted by the number of trajectories in the intensity histogram bin and the trajectory histogram bin, (iv) attenuated by ground-state decay calculated from the "travel time," and (v) added to the total line shape. This procedure is completed for all coordinates in the trajectory histogram, yielding the desired final line shape. Finally, the model line shape, which we define as $Y(\nu)$, is calculated for each of the 15 experimental resonances at the appropriate YAG pulse delay and excitation laser beam power.

The stated technique has several advantages over the more straightforward approach of integrating the atomic equations for each random trajectory; most important is a one- to two-order-of-magnitude increase in the calculation speed. Since the majority of the calculational effort is the integration of the coupled differential equations, binning trajectories with nearly identical intensities and pulse widths eliminates redundant integrations. In addition, once the line-shape table is generated, the geometry of the model may be changed and the new model line shape calculated without requiring any further numerical integrations. Thus, in a few minutes a line shape may be calculated with roughly a factor of 3 smaller statistical error than the best experimental line. Figure 11 shows the calculated model line shapes calculated at a Ps temperature of 576 K, at the five photoionization beam delays used in our measurements. The effect of the second-order Doppler shift is apparent in the redshift and asymmetry of the lines at short delay.

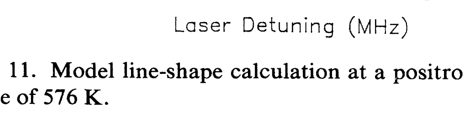

FIG. 11. Model line-shape calculation at a positronium temperature of 576 K.

IV. DATA REDUCTION AND DISCUSSION

A. Model fit to experimental resonances

In Fig. 12 we show five experimental resonances. Figure 13 shows two resonances taken at a low laser power of 0.7 and 1.0 kW for Stark-shift analysis. For each experimental resonance, model line shapes were calculated with the corresponding YAG delay and cw laser intensity. The only model parameters adjusted in the fit are the excitation amplitude and the center frequency for each of the resonances. For each experimental resonance, there were as many as 11 scans with 41 frequencies per scan in 5-MHz intervals. The number of photoionization events $n_i(\nu_i)$ observed with the laser set at frequency ν_i during the ith frequency step ($i=1$ to N, $N=451$), was determined from the time spectrum recorded for each interval. The calculated line shape $Y(\nu)$ is multiplied by a signal amplitude parameter a, and shifted to a frequency $\Delta\nu$ relative to the measured tellurium reference line. The fit is made by adjusting the parameters a and $\Delta\nu$ to maximize the Poisson likelihood estimator [65]

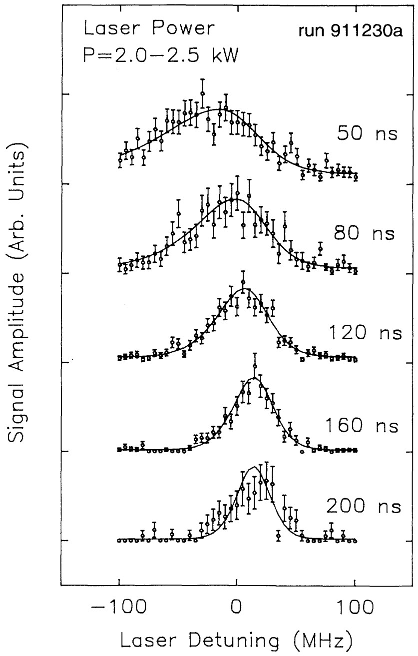

FIG. 12. Fit of the model line shape to five Ps resonances taken at different YAG photoionization pulse delays. The data in this figure were taken at a target temperature of 576 K and a cw laser power between 2 and 2.5 kW. For each resonance, there are two fit parameters. The model line shape at each YAG delay is multiplied by a signal amplitude parameter a and a frequency offset $\Delta\nu$ between the model Ps resonance frequency and the Te_2 line. The model fit adjusts only these two parameters.

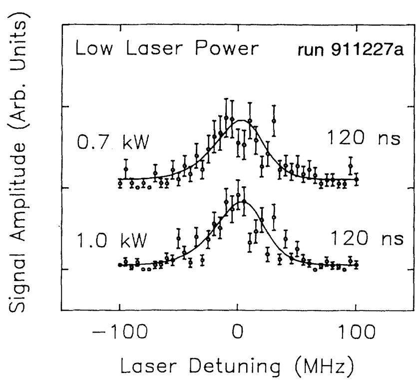

FIG. 13. Fit of the model line shape to two Ps resonances measured with a 120-ns YAG delay and a cw laser power of 0.7 and 1.0 kW for Stark shift analysis. The count rate was 4–5 times lower as the 120-ns data shown in Fig. 12.

$$P=\sum_{i=1}^{N}-ay_i(\nu_i-\Delta\nu)+n_i(\nu_i)\ln[ay_i(\nu_i-\Delta\nu)]-\ln n_i(\nu_i)!\ . \tag{28}$$

The calculated model line shape $Y(\nu)$ is interpolated to find its value at each frequency $\nu=\nu_i-\Delta\nu$. The model result is scaled by the beam strength (γ_i) measured during each frequency step, and added to a measured background count rate $(b\gamma_i)$, as determined from the CEMA time spectra, to yield the frequency-shifted model result:

$$y_i(\nu_i-\Delta\nu)=\gamma_i[Y(\nu_i-\Delta\nu)+b]\ . \tag{29}$$

Successive maximization of P in these two nearly independent fitting parameters converges to a global maximum after a few iterations.

For clarity, in Fig. 12 the best-fit model curves shown are simply added to a constant background and not scaled by the beam strength, while the experimental points shown are the sum of all counts at the given frequency. The error bars are simply the square root of the total counts. The data for all resonances were normalized to the same amplitude to emphasize the line shapes. The fitting procedure was applied to all 15 of the 600-K data sets.

The statistical uncertainties in the frequency and amplitude fits are determined from a Monte Carlo calculation in which the model was first fit to the experimental resonance to determine the best value of a and $\Delta\nu$. The model result at each frequency was then used as the mean value in a Poisson random number generator to create 2000 simulated "resonances" [57], to each of which the model calculation was refit. The distribution of the 2000 values of P_{MC} [from Eq. (28)], $\Delta\nu$, and a, resulting from fits to the Monte Carlo resonances, are used to determine the corresponding uncertainties for each of these variables. The distribution of P_{MC} is useful to determine the "goodness of fit" of the model line to an experimental resonance. If the value of P for a fit to a particular experimental resonance lies outside the distribution of P_{MC} for the Monte Carlo fits, the model may be an incorrect representation of the experiment. The values of P for all 15 measured resonances are in good agreement with the Monte Carlo results, with $\chi^2/(N-2)=1.04$ for $N=15$.

The fit of the model result to the experimental resonance allows us to estimate the Ps production rate. The 160-ns resonance in Fig. 12 has a maximum of 50 counts per 10^3 positron pulses, corresponding to 4000 Ps atoms per pulse according to the modeled excitation efficiency. Assuming a Ps production efficiency of 30% and a 50% YAG photoionization efficiency, we estimate an incident flux of 1.3×10^4 positrons per pulse in the skimmed beam, a factor of 2.5 lower than the original estimate of the source output [34] (assuming up to 50% loss from the skimmer).

B. Determination of the positronium $1\,^3S_1-2\,^3S_1$ interval

If there were little uncertainty in the model parameters, and the experiment were perfectly modeled, the fit line centers would be identical within statistical variations. Under such ideal conditions, the most appropriate strategy for determining the Ps line center would be to simultaneously fit the experimental resonances to the model with an overall amplitude and overall frequency offset by including all 15 resonances under the sum in Eq. (27). However, a deficiency in the model will only be apparent if each resonance is fit separately, and is indicated by variations in the fit centers as a function of two experimental parameters we varied: the laser power (P_0), and the photoionization pulse delay (Δt).

We first discuss the results of the data taken at a target temperature of 576 K. The largest contribution to the systematic errors in our measurement is the second-order Doppler shift, which is closely related to the Ps velocity distribution. We have an independent check on our assumption that the distribution is beam Maxwellian since the signal strength observed at different YAG photoionization delays is also dependent on the velocity distribution of the Ps atoms. In Fig. 14(a) we show the signal amplitude parameter a plotted versus the Ps energy, estimated from the YAG delay (Δt) as

$$E_{\mathrm{Ps}}\propto\frac{1}{2}\left[\frac{0.4\ \mathrm{cm}}{c\,\Delta t}\right]^2\times10^9\ \mathrm{meV}\ . \tag{30}$$

We can see that the fit amplitude parameter is constant within $\sigma=10\%$ for all of the data taken, indicating that the model and experimental Ps velocity distributions are nearly identical over an order of magnitude in Ps energy. Figure 14(b) shows that the model amplitudes also have the correct dependence on circulating laser power. If we reduce the model Ps excitation probability by a factor of 2, the fit amplitudes are still consistent with a constant, indicating that we were not saturating the 1S-2S transition for most atoms during the experiment.

Figure 15(a) shows 13 fit line centers plotted as a function of approximate positronium energy for the set of model parameters we believe to be representative of the geometry of the experiment. The data have a small residual slope of 141±124 MHz/eV, 1.13 standard deviations above zero. To account for possible overcorrection of the

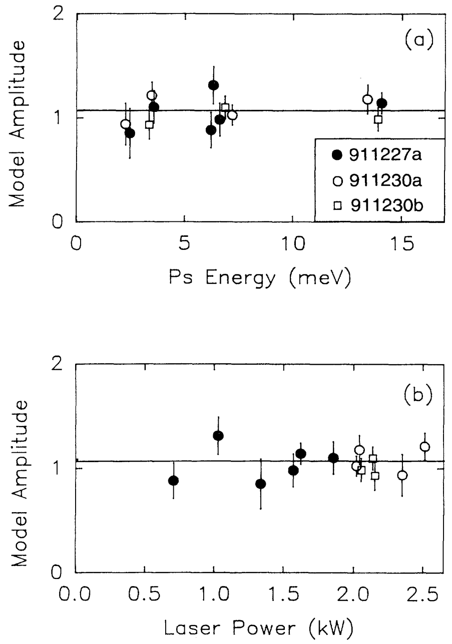

FIG. 14. (a) Signal amplitude parameter *a* for each of the 15 model fits plotted as a function of positronium energy for a set of model parameters we believe to be representative of the geometry of the experiment. The amplitudes of the model lines agree with the strength of the experimental resonances to roughly 10% over an order of magnitude in Ps energy, validating our assumption of a beam Maxwellian velocity distribution. The filled circles, hollow circles, and squares represent results from separate data taking runs. (b) Signal amplitude parameter for all 15 model fits plotted as a function of laser beam power for the same model parameters as in (a). The agreement between our model lines and the observed resonances to 10% indicates that the laser power dependence of the transition is correctly modeled.

second-order Doppler shift, we extrapolate linearly to zero Ps energy to find the Ps resonance frequency. We note that the fit line centers are also perfectly consistent with their weighted mean of 10.04±0.46 MHz. The reduced χ^2 parameter of the data to the mean is $\chi^2=0.5$, indicating that the scatter in the line centers is actually $\sqrt{2}$ smaller than expected based on our Monte Carlo statistical error estimate. The extrapolation is a more conservative approach, giving a statistical uncertainty of 0.90 MHz, compared to a 0.46-MHz uncertainty in the weighted mean. We discuss later the results of the data analysis for each of these techniques.

The line centers of the two scans taken at the shortest time delay ($\Delta=50$ ns), corresponding to an energy of 43 meV, fall roughly 5 MHz to the red of the others and are not plotted in Fig. 15. The implication of the discrepancy may be that the model line shape at this delay is 5 MHz too far to the blue. Looking at Fig. 12, one can see that a significant fraction of the red tail of the 50-ns resonances falls outside of the scan range of our experimental apparatus. Thus, the inconsistency may result from attempting to fit the model to a truncated experimental resonance. As a result, we choose not to use the two 50-ns scans in our data analysis.

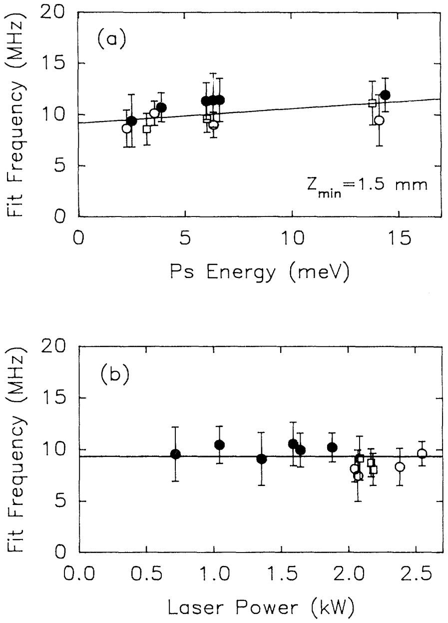

FIG. 15. (a) Frequency of fit line centers relative to the tellurium reference line plotted as a function of approximate positronium energy for the same model parameters used in Fig. 14. The fit line centers for the 13 scans shown lie on a line. If the model accounted ideally for the photoionization geometry, the slope of this line would be zero. However, using the calculated statistical uncertainty in the individual frequency fit results, the slope of the line is 141(124) MHz/eV. To account for the residual second-order Doppler shift, we extrapolate this line to zero positronium energy to find the true line center. (b) The frequency of the fit line centers relative to the tellurium reference line is plotted as a function of the measured circulating power in the excitation beam. One can see that the fits are consistent with a horizontal line, indicating that the model has correctly accounted for the ac Stark shift of the line shape.

The fit line centers are plotted as a function of the measured circulating power in the excitation beam in Fig. 15(b). The slope of the fits is consistent with zero because the model has correctly accounted for the ac Stark effect over a fraction-of-3 variation in the laser intensity. Our laser power measurement is sufficiently accurate that it contributes less to the uncertainty in the slope of these fits than does the statistical error. It is therefore not necessary to extrapolate the fits to zero laser intensity in the determination of the Ps line center.

There are, of course, uncertainties in our measurements and estimates of the various model parameters, which will contribute to the uncertainty in our measurement of the Ps transition relative to tellurium. For example, there is some uncertainty in our estimate of the distance between the Ps source and the nearest edge of the photoionization beam because of irregularities in the shape of the 532-nm beams. There is also uncertainty as to what diameter and ellipticity to use in the elliptical model of the YAG beams to most accurately represent the experiment. By calculating the model line shapes

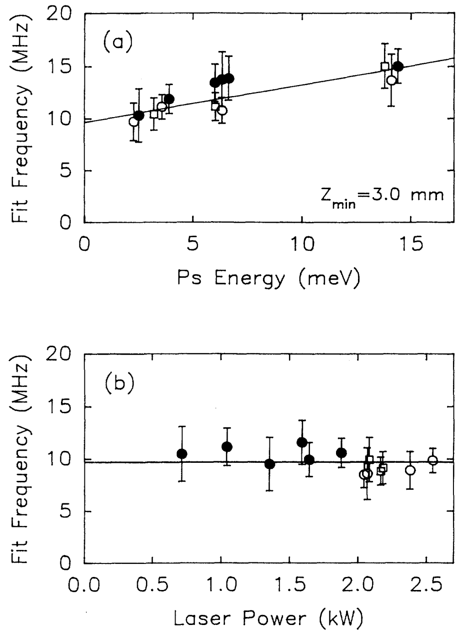

FIG. 16. (a) Fit line centers for 13 experimental resonances as a function of the mean positronium energy with the photoionization region placed away from the target 3 mm. The increased distance results in a faster ensemble of atoms sampled after a given time delay, and a corresponding redshift in the model line centers. For this unlikely setting of the model parameters the model overcorrects for the second-order Doppler shift of the experimental resonances, as seen by the increased slope of 360(124) MHz/eV. Note that the zero-energy intercept of the fit line is nearly identical in Fig. 15(a) and (a) of this figure. (b) Fit line centers plotted as a function of circulating laser power for the model parameters in (a). There is little change in the slope of these data for the different YAG parameters.

with a range of these parameters, and fitting to the experimental resonances, we can determine the corresponding variation in the estimated positronium line center. Figure 16(a) shows the fit line centers for the 13 experimental resonances as a function of the mean positronium energy with the nearest edge of the photoionization region in our model placed 3 mm from the target, resulting in a faster ensemble of atoms sampled at a given YAG delay, and a corresponding redshift in the model line centers. The fact that the model overcorrects for the second-order Doppler shift of the experimental resonances is apparent in the increased slope of a line fit through the points. Note, however, that the zero-energy intercept of the fit line is nearly identical in both cases, as one might expect.

It is not generally the case, however, that the extrapolated line center is constant as various model parameters are varied. In the upper row of Figs. 17(a)–17(d), we show the extrapolated line center as a function of four model parameters related to the YAG beams. The extrapolated frequency was calculated as the parameters were varied one at a time from the values indicated by the solid points. The vertical bars below the curves represent our full 67% confidence interval in the value of the parameter. The horizontal bars show the contribution of the given parameter to the uncertainty in the frequency determination. The bottom row of graphs in Figs. 17(a)–17(d) show the slope of the fit frequencies versus Ps energy from Fig. 15(a) as a function of the model parameters. The extrapolated Ps line center shows particular sensitivity to the YAG beam ellipticity and photoionization region height as defined by the vertical CEMA apertures. The contribution of these parameters to the final frequency uncertainty is the largest of the four.

In the upper row of Figs. 17(e)–17(g), we show the extrapolated Ps line center versus three additional parameters. The line center shows little sensitivity to the Ps temperature. As expected, the line center shows some sensi-

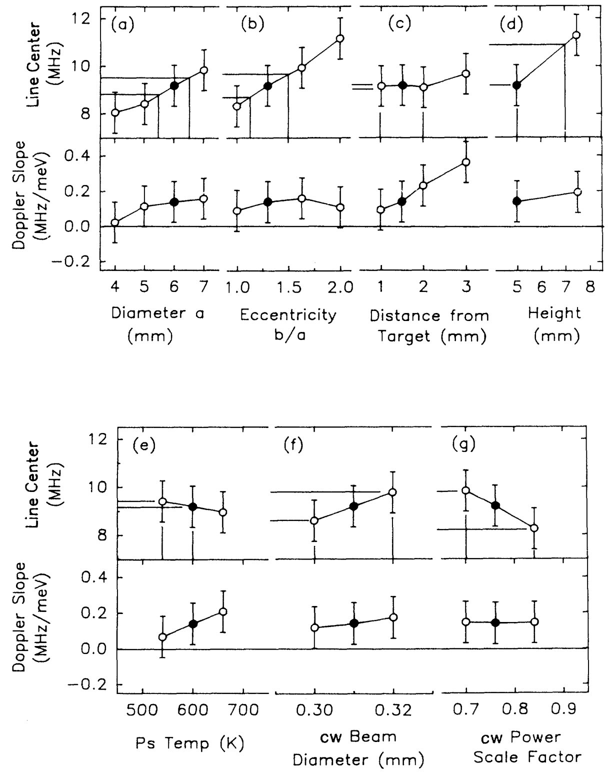

FIG. 17. Extrapolated line center vs several model parameters. The contribution of our uncertainty in the model parameters to the quoted uncertainty in our measurement of the Ps line center relative to the Te_2 line is determined by plotting the extrapolated Ps line center relative to the Te_2 line for a range of model parameter values. For each parameter, our estimate of the full 67% confidence interval in the parameter value is marked by the vertical bars, and the corresponding confidence interval in the frequency offset is marked by the horizontal bars. Also shown in each figure is the Doppler slope of the line used to extrapolate the fit line centers to zero energy. The frequency confidence intervals are tabulated in Table III. The six parameters plotted are (a) YAG beam diameter, (b) YAG beam eccentricity, (c) distance from YAG beam edge to target, (d) photoionization region height, (e) positronium temperature, (f) cw beam diameter, (g) power scale factor, from the calibration of the cw laser power. The first four of these parameters influence the size of the second-order Doppler shift distribution, and the last two affect the ac Stark shift calculation.

tivity to the two parameters that affect the ac Stark-shift correction: the cw beam diameter, and the power scale factor defined in Sec. II G. The systematic uncertainty for each of these parameters is entered in Table III. The net systematic uncertainty is 1.23 MHz, and the statistical uncertainty is 0.9 MHz for the extrapolated line center.

The weighted mean of the fit line centers of the 13 resonances has also been calculated for the same variations in the model parameters just discussed. In general, adjusting the model YAG beam parameters affects the line center of the fast positronium atoms more than the slow atoms, causing the mean fit line center to be more sensitive to these changes than the extrapolated line center. As a result, the determination of the Ps 1*S*-2*S* line center using the weighted means has a larger net systematic uncertainty of 1.50 MHz. The statistical uncertainty for the weighted mean is 0.46 MHz, smaller than for the extrapolated line center. There is a nearly identical final uncertainty in the Ps 1*S*-2*S* interval for the extrapolation and the weighted mean, with a 1.0-MHz higher result for the transition frequency using the weighted mean.

The reduction of our measurements to an absolute value for positronium $1\,^3S_1-2\,^3S_1$ interval is detailed in Table III. The first row shows the results of the calibration our tellurium cell relative to the hydrogen 1*S*-2*S* transition frequency, followed by the +55.0-MHz offset of the observed tellurium frequency introduced by the 110-MHz AOM. The third line shows the Ps line-center measurements relative to the Te_2 line determined from the fit of the computer model. As discussed above, residual error in the line center due to uncertainty of various model parameters is determined by varying these parameters and noting the effect on the fit line center. The most important parameters, the error in the parameter, and the corresponding error in the frequency determination are listed in the next few rows of the table. The final uncertainty in the determination of the Ps line center relative to the observed tellurium line is 1.5 MHz. Finally, the dc Stark shift due to the ~2 V/cm accelerating field is calculated to be −0.07 MHz with 100% uncertainty due to the nonuniform electric field near the target.

The Zeeman shift of the $1\,^3S-2\,^3S$ $(m=0\rightarrow 0)$ transition is 3.42 MHz in the 150-G field [66,67]. Because of the opposite magnetic moments of the positron and electron, there is no Zeeman shift of the $m=\pm 1$ states, even at the level of relativistic contributions to the electron and positron *g* factor. Thus, if we assume a statistical population in each of the three magnetic sublevels, the Zeeman effect produces a +1.14-MHz shift in the observed Ps resonance. In future measurements of the Ps 1*S*-2*S* transition, with linewidths approaching the 1.26-MHz natural linewidth, the contribution to the line center due to Zeeman shift of the $m=0$ states may be eliminated by operating at a large enough magnetic field (~300 G) to completely separate the shifted $m=0\rightarrow 0$ transition from the unshifted $m=\pm 1\rightarrow 1$ transitions. There is a small energy shift of the $2\,^3S_1$ $(m=\pm 1)$ states due to the motional Stark shift. As the atom moves in the magnetic field, it experiences an electric-field proportional to $\mathbf{E}\propto\mathbf{v}\times\mathbf{B}$ which Stark shifts the energy levels. The motional Stark shift in the 150-G magnetic field is calculated to be 0.5 MHz at Ps kinetic energy of 25 meV [67] and is eliminated by our extrapolation procedure.

TABLE III. Summary of uncertainties and results.

Te_2 reference line			616 803 544.4±0.6 MHz
AOM offset			55.0±0.0
Model fit to line center			10.0±1.5
Statistical uncertainty		±0.9	
YAG parameters			
diameter *a*:	6.0±0.5 mm	±0.3	
eccentricity *b/a*:	1.3±0.2	±0.5	
distance from target:	1.5±0.5 mm	±0.1	
height:	6.0±1.0 mm	±0.8	
Ps temperature:	576±30 K	±0.2	
cw beam diam:	0.31±0.01 mm	±0.3	
cw power meas:	761±38 W/V	±0.5	
dc Stark shift	−0.07±0.1		
Quadratic Zeeman shift	−1.14±0.0		
1*S*-2*S* transition frequency			616 803 608.2±1.6 MHz
1*S*-2*S* interval			1 233 607 216.4±3.2
Previous measurement			
Chu, Mills, Jr., and Hall [2]; Danzmann, Fee, and Chu [31]			1 233 607 218.9±10.7
Theory			
Fell [14]			1 233 607 221.7±O(10)

With these corrections, the absolute transition frequency is found to be 616 803 608.2±1.6 MHz.

V. CONCLUSIONS

We obtain a result for the $1\,^3S_1-2\,^3S_1$ interval in positronium of 1 233 607 216.4±3.2 MHz, in agreement with the most recent $R_\infty\alpha^4\ln\alpha$ QED corrections of Fell [14] yielding a theoretical value of 1 233 607 221.7±$O(10)$ MHz. Our measured value is 2.5 MHz lower and in good agreement with the corrected value of the Chu-Mills-Hall measurement [2,31]. The precision of the measurement reported in this paper is sufficient to test the as-yet-uncalculated $R_\infty\alpha^4$ QED corrections to both the excited and ground states, which are estimated to be on the order of 10 MHz. Our measurement tests the α^2R_∞ QED contribution to the energy levels of the $1\,^3S_1$ and $2\,^3S_1$ states to 3.5 parts in 10^5.

The agreement between our experimental result and theory represents an improved measurement of the positron-electron mass ratio [32,2,23]. In the comparison of the QED prediction with experiment, one implicitly assumes that the positronium Rydberg constant is exactly half the hydrogen Rydberg constant. The agreement between theory and our experiment at the level of ±10 MHz places a limit on the positron-electron mass difference on the order of $\Delta m/m=8\times10^{-9}$. If agreement with theory persists with the $R_\infty\alpha^4$ QED correction in progress, our present measurement will place a constraint of $\Delta m/m=2\times10^{-9}$ on the e^+-e^- mass ratio, the best limit on a particle-antiparticle mass ratio apart from the K^0-$\bar{K}^0$ system. Hughes and Deutch [68] point out that the measurement of the Ps 1S-2S interval also constrains the positron-electron charge ratio. They use the measured ratio of the positron and electron cyclotron frequencies [33] to eliminate the e^+-e^- mass ratio in the expression for the ratio of the positronium and hydrogen Rydberg constants. The result is an expression for the uncertainty in the charge ratio in terms of the uncertainty in the ratio of cyclotron frequencies and the uncertainty in the Rydberg-constant ratio. The result, $q_e/q_{e^+}=1\pm2.5\times10^{-8}$, is limited entirely by the 130-ppb uncertainty in the cyclotron frequency ratio. With a factor of 100 improvement in the measurement of the cyclotron ratio, the result would be limited by the positronium 1S-2S measurement at the level of 1×10^{-9}.

Further improvements over our measurement of the $1\,^3S_1-2\,^3S_1$ are clearly possible. Although we were not able to make this measurement using a cold positronium source, there is evidence that such a source can be made, albeit with a reduced Ps yield. Cold Ps would greatly reduce the second-order Doppler shift and the transit-time broadening of the observed resonances. Since the excitation probability scales roughly as the square of the both the interaction time and the laser intensity, a factor of 10 reduction in temperature and a factor of 3 lower laser intensity would yield the same signal. The ac Stark shift would be concomitantly reduced to roughly 6 MHz from the 18 MHz of the present measurement. It is clear that a measurement of the 1S-2S transition might reach a precision better than the 1.3 MHz natural linewidth with apparatus similar to that described in this thesis.

An alternative technique of detecting excited-state Ps atoms by photoionization is direct detection of excited-state atoms at a CEMA. The strong electric fields in the channels of the CEMA would couple the 2S and 2P states, causing the emission of a Lyman-α photon at 243 nm. The 243-nm photon would then be detected with a high probability. There is a potential signal-to-noise problem since the detection probability for γ rays from the positronium source is roughly 10^{-4}, nearly the same as the excitation probability per Ps atom we observed in the present experiment. The use of a submillimeter Ps source size would improve the excitation probability per Ps atom by as much as an order of magnitude over the 10-mm-diam source used here.

An additional advantage of a small source is that, in conjunction with a spatially resolved CEMA, by knowing the time and position of the beginning and end of each Ps trajectory one could accurately determine the second-order Doppler shift of each detected atom. The advantages in measurement precision accrued by this approach would be significantly greater with a concomitant reduction in Ps temperature.

It is possible that a future measurement of the Ps 1S-2S transition can be made using a ^{22}Na β^+ source. Beam time constraints at an accelerator facility can be detrimental to the requirements of making a precision measurement. Recently a positron flux of 5×10^6 slow positrons per second has been obtained [69] using a solid Ne moderator [70] and a 70-mCi ^{22}Na source. The improved efficiency of the solid Ne moderator makes possible yields larger by a factor of 10 than with a tungsten moderator. The continuous radioactive source would be particularly useful if the direct detection of excited-state Ps atoms at a CEMA detector worked effectively. If not, various bottling and trapping schemes may be considered to reduce the duty cycle of the source while maintaining a useful average flux. Laser cooling, discussed below, would almost certainly require a pulsed source of positronium atoms at the same repetition rate as the high-intensity cooling laser.

The ultimate reduction in the positronium temperature would, of course, be achieved by laser cooling the atoms. Subkelvin positronium temperatures may be possible with laser cooling techniques. The laser cooling of positronium presents an unusual challenge since (i) the ground-state atom annihilates in 140 ns, (ii) the Doppler width at room temperature is ~500 GHz, and (iii) the single photon recoil velocity corresponds to a Doppler shift of 6.1 GHz. Thus, the "chirped slowing" commonly used for heavier atoms is not feasible. Even if it were possible to generate a frequency chirp of 500 GHz in 140 ns, the random recoil due to the spontaneous emission could easily give the atom a velocity that would Doppler shift the laser to the blue side of the resonance.

We consider a white-light cooling scheme that is a modification of a scheme proposed by Hoffnagle [71], and discussed for Ps by Liang and Dermer [72]. The theory of broadband laser cooling on narrow transitions was explored in detail by Wallis and Ertmer [79]. The idea is to irradiate the atoms with a quasicontinuum radiation that is to the low-frequency side of the $1S$-$2P$ frequency. The radiation spectrum is designed to drop off sharply (compared to the recoil Doppler shift) at the resonance frequency. Atoms moving toward any particular laser beam will be Doppler shifted into resonance and will scatter radiation until its velocity is reversed. By including a counter-propagating laser beam that will be Doppler shifted into resonance as the atom reverses direction, the cooling would work in a similar fashion to the usual optical molasses. In the usual molasses, however, the cooling limit is determined solely by the atomic linewidth, which is much larger than the recoil Doppler shift. For positronium cooling, the temperature limit is given by the spectral distribution of the cooling laser and ultimately by the recoil velocity (~ 6.1 GHz), which is much larger than the transition linewidth of 50 MHz.

The "white light" could be obtained by constructing a FM laser [73], where modulation depths of 1000 are easily produced [74]. A modulation frequency of 150 MHz will result in a laser frequency varying sinusoidally over a range of 150 GHz. The FM laser beam would then be amplified in a series of traveling-wave amplifiers and then frequency doubled in a β-barium borate crystal which can phase match to the 150 GHz simultaneously. An inherent characteristic of the FM laser technique is that the edge of the resulting spectral distribution falls off in ~ 3 GHz, less than the 6-GHz single-photon recoil shift. The lifetime of the $2P$ state is 3.2 ns, so with a FM modulation frequency of 150 MHz, the laser frequency sweeps over the $1S$-$2P$ transition roughly once per $2P$ lifetime.

Beginning with atoms at 50 K, we would need only ~ 18 photon kicks to cool the atoms to the recoil limit. We estimate a one-dimensional cooling time of 130 ns. In three dimensions, the situation is more complicated. The stimulated redistribution of photons among the three resonant beams will increase the cooling time by perhaps a factor of 3 to roughly 400 ns. For rapid slowing, however, the $1S$-$2P$ transition must be nearly saturated, increasing the Ps lifetime to ~ 250 ns because the atom spends half of its time in the nonannihilating $2P$ state. At shorter cooling times, one slows a correspondingly smaller fraction of the initial thermal distribution, emphasizing the importance of starting with as cold an initial thermal distribution as possible.

Due to annihilation, there is clearly an optimum duration of the cooling pulse after which the number of cooled atoms remaining does not increase. The long cooling pulses required are not trivial to generate. One possibility is to frequency double the 20-ns pulse of an excimer pumped amplifier and stretch the doubled light by a factor of 16 using several stages of delay lines [75–77].

We estimate a final recoil limited temperature of <0.4 K, which gives a second-order Doppler width of only ~ 50 kHz, and a transit time broadening in a cw laser beam similar to the one used in the present measurement of ~ 300 kHz. Of course, the linewidth of the transition would be dominated by the 142-ns ground-state lifetime. The 20-fold increase in interaction time over the present experiment would allow a cw beam intensity of only 100 kW/cm^2 to be used, resulting in an ac Stark shift of the Ps line center of only 1 MHz. It is possible that the 1-MHz resonance width could then be split by a factor of 10 to 100 by a careful study of the systematic effects.

At the level of 10–100 kHz, the tellurium frequency standard used in this paper will clearly not be adequate. One solution is to compare the $1S$-$2S$ energy difference in Ps to the $n=2$ to 4 transition in deuterium, ~ 114 GHz from half of the Ps transition frequency. A circulating power of 50 W of 972-nm radiation in a build-up cavity has been shown to produce a 5% dip in a hydrogen metastable ($2S$) beam by two-photon excitation of the $2S$-$4S$ transition [78].

It is difficult to detect the 114-GHz beat note produced by doubling the 972-nm light and mixing it with the 486-nm light of the Ps spectrometer. An alternative might be to frequency double the output of a (second) diode laser at 972 nm and phase lock the diode laser to the 486-nm light of the Ps spectrometer. The 57-GHz beat note between the deuterium spectrometer laser and the intermediate 972-nm diode can easily be detected with commercial detectors. Recently, the deuterium $2S$-$4S$ transition frequency has been measured [78] to an accuracy of ~ 10 kHz, providing a suitable frequency reference for any presently conceivable measurement of the positronium $1\,^3S_1-2\,^3S_1$ interval.

ACKNOWLEDGMENTS

We would like to acknowledge the vital assistance of T. W. Hänsch and F. Schmidt-Kaller in calibrating our tellurium cell, R. G. DeVoe for assistance with the supercavity lock, and C. E. Wieman, J. L. Hall, and S. Brodsky for helpful discussions. This work was supported in part by a NIST Precision Measurements Grant and the National Science Foundation.

---

*Present address: AT&T Bell Laboratories, Murray Hill, NJ 07974.

[1] E. Klempt, in *The Hydrogen Atom*, edited by G. F. Bassani, M. Inguscio, and T. W. Hänsch (Springer-Verlag, Pisa, 1988), p. 211.
[2] S. Chu, A. P. Mills, Jr., and J. L. Hall, Phys. Rev. Lett. **52**, 1689 (1984).
[3] S. Chu *et al.*, Phys. Rev. Lett. **60**, 101 (1988).
[4] E. E. Salpeter and H. A. Bethe, Phys. Rev. **84**, 1232 (1951).
[5] J. Schwinger, Proc. Natl. Acad. Sci. USA **37**, 452 (1951).
[6] W. E. Caswell and G. P. Lepage, Phys. Rev. A **18**, 810 (1978).
[7] R. Barbieri and E. Remiddi, Nucl. Phys. **B141**, 413 (1978).
[8] S. Klarsfeld and A. Maquet, Phys. Lett. **43B**, 201 (1973).
[9] R. A. Ferrell, Phys. Rev. **84**, 858 (1951).
[10] T. Fulton and P. C. Martin, Phys. Rev. **95**, 811 (1954).

[11] T. Fulton, Phys. Rev. A **26**, 1794 (1982).
[12] S. N. Gupta, W. W. Repko, and C. J. Suchyta III, Phys. Rev. D **40**, 4100 (1989).
[13] J. R. Sapirstein and D. R. Yennie, in *Quantum Electrodynamics,* edited by T. Kinoshita (World Scientific, Singapore, 1990), p. 560.
[14] R. N. Fell, Phys. Rev. Lett. **68**, 25 (1992).
[15] I. B. Khriplovich, A. I. Milstein, and A. S. Yelkhovsky, Phys. Lett. B **282**, 237 (1992). An initial disagreement with Ref. [14] has been resolved and the result of Ref. [14] appears to be correct [R. N. Fell (private communication)].
[16] A. P. Mills, Jr. and S. Chu, in *Quantum Electrodynamics* (Ref. [13]), p. 774.
[17] S. Adachi *et al.*, Phys. Rev. Lett. **65**, 2634 (1990).
[18] J. S. Nico, D. W. Gidley, A. Rich, and P. W. Zitzewitz, Phys. Rev. Lett. **65**, 1344 (1990).
[19] W. G. Caswell and G. P. Lepage, Phys. Rev. A **20**, 36 (1979).
[20] G. S. Adkins, Ann. Phys. (N.Y.) **146**, 78 (1983).
[21] L. S. Vasilenko, V. P. Chebotaev, and A. V. Shishaev, Pis'ma Zh. Eksp. Teor. Fiz. **12**, 161 (1970) [JETP Lett. **12**, 113 (1970)].
[22] B. Cagnac, G. Grynberg, and F. Biraben, J. Phys. (Paris) **34**, 845 (1973).
[23] S. Chu and A. P. Mills, Jr., Phys. Rev. Lett. **48**, 1333 (1982).
[24] D. H. McIntyre and T. W. Hänsch, Phys. Rev. A **34**, 4504 (1986).
[25] E. A. Hildum, U. Boesl, D. H. McIntyre, R. G. Beausoleol, and T. W. Hänsch, Phys. Rev. Lett. **56**, 576 (1986).
[26] C. Wieman and T. W. Hänsch, Phys. Rev. A **22**, 192 (1980).
[27] M. S. Fee, K. Danzmann, and S. Chu, Phys. Rev. A **45**, 4911 (1992).
[28] A. P. Mills, Jr. *et al.*, Phys. Rev. B **44**, 5791 (1991).
[29] R. G. DeVoe (private communication).
[30] R. Kallenbach, C. Zimmerman, D. H. McIntyre, T. W. Hänsch, and R. G. DeVoe, Opt. Commun. **70**, 56 (1989).
[31] K. Danzmann, M. S. Fee, and S. Chu, Phys. Rev. A **39**, 6072 (1989).
[32] E. W. Weber, in *Present Status and Aims of Quantum Electrodynamics,* edited by G. Gräff, E. Klempt, and G. Werth (Springer-Verlag, Berlin, 1981), Vol. 143, p. 146.
[33] P. B. Schwinberg, R. S. VanDyck, and H. G. Dehmelt, Phys. Lett. **81A**, 119 (1981).
[34] A. P. Mills, Jr., E. D. Shaw, R. J. Chichester, and D. M. Zuckerman, Rev. Sci. Instrum. **60**, 825 (1989).
[35] A. P. Mills, Jr. and L. Pfeiffer, Phys. Rev. B **32**, 53 (1985).
[36] R. W. P. Drever *et al.*, Appl. Phys. B **31**, 97 (1983).
[37] G. C. Bjorklund, Opt. Lett. **5**, 15 (1980).
[38] J. L. Hall, L. Hollberg, T. Baer, and H. G. Robinson, Appl. Phys. Lett. **39**, 680 (1981).
[39] C. Bordé, C. R. Acad. Sci. **271**, 371 (1970).
[40] P. W. Smith and T. W. Hänsch, Phys. Rev. Lett. **26**, 740 (1971).
[41] R. H. Powell, R. A. Alvarez, and M. Stanek, Appl. Phys. Lett. **40**, 751 (1982).
[42] A. Vehanen, K. G. Lynn, P. J. Schultz, and M. Eldrup, Appl. Phys. A **32**, 163 (1983).
[43] A. P. Mills, Jr., in *Positron Scattering in Gases,* edited by J. W. Humberston and M. R. C. McDowell (Plenum, New York, 1984), p. 121.
[44] P. J. Schultz and K. G. Lynn, Rev. Mod. Phys. **60**, 701 (1988).
[45] A. P. Mills, Jr., Appl. Phys. **22**, 273 (1980).
[46] A. P. Mills, Jr., Solid State Commun. B **1**, 623 (1979).
[47] A. P. Mills, Jr., Phys. Rev. Lett. **41**, 1828 (1978).
[48] A. P. Mills, Jr. and S. Chu, in *Atomic Physics 8,* edited by A. Rosen and S. Svanberg (Plenum, New York, 1982).
[49] A. P. Mills, Jr. *et al.*, Phys. Rev. Lett. **66**, 735 (1991).
[50] M. S. Fee *et al.*, Phys. Rev. A **44**, R5 (1991).
[51] D. H. McIntyre, W. M. Fairbank, Jr., S. A. Lee, T. W. Hänsch, and E. Riis, Phys. Rev. A **41**, 4632 (1990).
[52] G. P. Barwood, W. R. C. Rowley, P. Gill, J. L. Flowers, and B. W. Petley, Phys. Rev. A **43**, 4783 (1991).
[53] T. Andreae *et al.*, Phys. Rev. Lett. **69**, 1923 (1992).
[54] J. R. M. Barr *et al.*, Opt. Commun. **54**, 217 (1985).
[55] J. D. Gillaspy and C. J. Sansonetti, J. Opt. Soc. Am. B **8**, 2414 (1991).
[56] J. L. Hall (private communication).
[57] W. H. Press, B. P. Flannery, S. A. Teukolsky, and W. T. Vetterling, *Numerical Recipes in Fortran* (Cambridge University Press, Cambridge, 1988).
[58] R. G. Beausoleil, Ph.D. thesis, Stanford University, 1986 (unpublished).
[59] A. E. Siegman, *Lasers* (University Science Books, Mill Valley, CA, 1986).
[60] C. Bordé, J. Spectrosc. B **282**, 341 (1976).
[61] F. Bassani, J. J. Forney, and A. Quattropani, Phys. Rev. Lett. **39**, 1070 (1977).
[62] C. R. Holt, M. G. Raymer, and W. P. Reinhardt, Phys. Rev. A **27**, 2971 (1983).
[63] S. A. Lee, Ph.D. thesis, Stanford University, 1975 (unpublished).
[64] H. A. Bethe and E. E. Salpeter, *Quantum Mechanics of One- and Two-Electron Atoms* (Plenum, New York, 1977), p. 306.
[65] L. Lyons, in *Statistics for Nuclear and Particle Physicists* (Cambridge University Press, Cambridge, 1986), p. 85.
[66] H. Grotch and R. Kashuba, Phys. Rev. A **7**, 78 (1973).
[67] M. L. Lewis and V. W. Hughes, Phys. Rev. A **8**, 625 (1973).
[68] R. J. Hughes and B. I. Deutch, Phys. Rev. Lett. **69**, 578 (1992).
[69] G. R. Brandes *et al.*, Mater. Sci. Forum **105-110**, 1359 (1992).
[70] A. P. Mills, Jr. and E. M. Gullikson, Appl. Phys. Lett. **49**, 1121 (1986).
[71] J. Hoffnagle, Opt. Lett. **13**, 102 (1988).
[72] E. P. Liang and C. D. Dermer, Opt. Commun. **65**, 419 (1988).
[73] S. E. Harris and R. Targ, Appl. Phys. Lett. **5**, 202 (1964).
[74] D. M. Kane *et al.*, in *Laser Spectroscopy VII* (Springer-Verlag, Berlin, 1985), p. 362.
[75] D. Herriott, H. Kogelnik, and R. Kompfner, Appl. Opt. **3**, 523 (1964).
[76] D. R. Herriott and H. J. Schulte, Appl. Opt. **4**, 883 (1965).
[77] W. R. Trutna and R. L. Byer, Appl. Opt. **19**, 301 (1980).
[78] M. Weitz, F. Schmidt-Kaler, and T. W. Hänsch, Phys. Rev. Lett. **68**, 1120 (1992).
[79] H. Wallis and W. Ertmer, J. Opt. Soc. Am. B **6**, 2211 (1989).

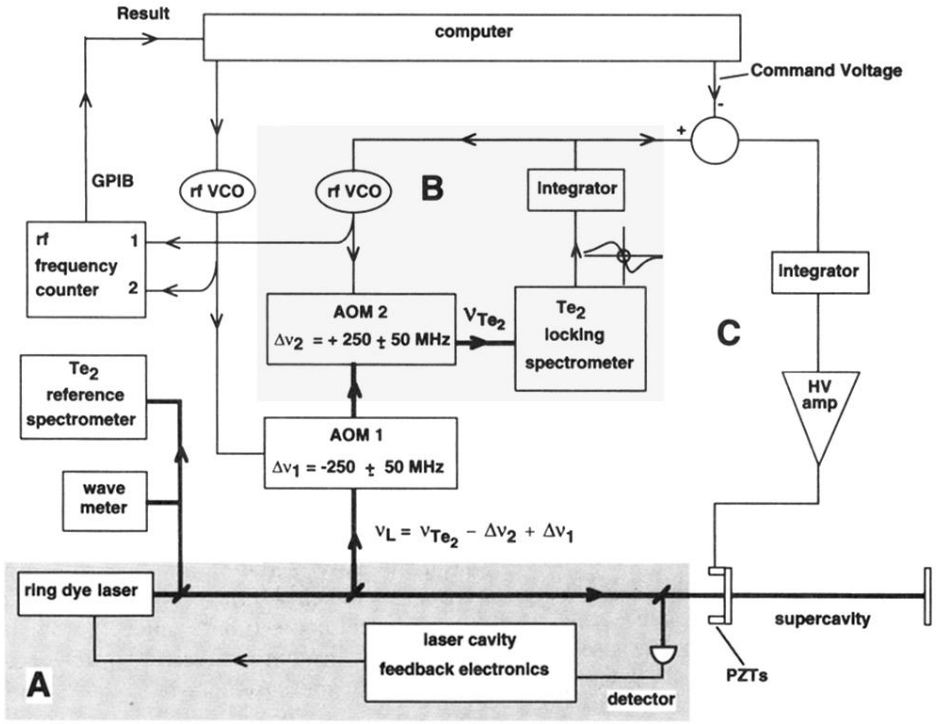

FIG. 6. Three main feedback loops operate simultaneously to allow highly linear frequency scans over a 200-MHz range. Loop *A* locks the ring-dye-laser frequency to the 2-kHz linewidth of the build-up cavity. An rf sideband lock technique [36] provides a roughly 1-MHz servo bandwidth to modulate an intracavity phase modulator in the ring-dye laser. The result is a 100-Hz stability of the dye laser relative to the chosen build-up cavity resonance. Loop *B* locks the laser output of the acousto-optic modulator AOM no. 2 to the correct frequency such that the output of the locking spectrometer is held at 0 V. The integrated spectrometer output is used to control a radio-frequency (rf) voltage-controlled oscillator (rf VCO no. 2), which drives AOM no. 2. When the frequency-shifted beam reaches the correct frequency, the spectrometer output voltage is zero, and the integrator holds the control voltage constant. As the build-up cavity is piezoelectrically tuned, the dye-laser frequency follows due to lock *A* and the control voltage and modulation frequency of AOM no. 2 follow due to lock *B*. Lock *C* controls the high voltage on the build-up cavity piezoelectric tuning elements (PZT's) to force the control voltage V_{RF2} of rf VCO no. 2 to a preset value. The difference of V_{RF2} and a command voltage V_{com} provides an error signal which is integrated, and amplified sufficiently to drive the PZT's, forcing the error signal to zero. The frequency of the cavity resonance is then locked to the tellurium line with an offset determined by the command voltage V_{com} and a RMS stability of ± 0.2 MHz determined by the voltage-controlled oscillator and cavity vibrations. By varying the driving frequency of AOM no. 1, the range of our frequency scan is extended by a factor of 2.